Geochemistry, Geophysics, Geosystems

RESEARCH ARTICLE
10.1029/2020GC009230

A Novel Approach to Identifying Mantle-Equilibrated Zircon by Using Trace Element Chemistry

Ziqin Ni[1], Ricardo Arevalo Jr.[1], Philip Piccoli[1], and Barry L. Reno[2]

[1]Department of Geology, University of Maryland, College Park, MD, USA, [2]Northern Territory Geological Survey, Darwin, NT, Australia

Key Points:

- This study has established a multidimensional filter scheme to select mantle-equilibrated zircon using trace element chemistry alone
- The local melt redox states have been estimated from zircon using Ti-in-zircon thermometry and Ce/Ce* oxybarometry
- This proposed filter scheme has been validated with external datasets and derived mantle redox states around ΔFMQ since the early Earth

Supporting Information:

- Data Set S1
- Supporting Information S1

Correspondence to:
Z. Ni,
zni@umd.edu

Citation:
Ni, Z., Arevalo, R., Piccoli, P., & Reno, B. L. (2020). A novel approach to identifying mantle-equilibrated zircon by using trace element chemistry. *Geochemistry, Geophysics, Geosystems*, *21*, e2020GC009230. https://doi.org/10.1029/2020GC009230

Received 12 JUN 2020
Accepted 26 SEP 2020

Abstract One of the requirements for inferring mantle redox states via zircon Ce/Ce* oxybarometry and Ti-in-zircon thermometry is to select mantle-equilibrated zircon derived from melts that have not interacted with the hydrosphere nor assimilated exogenous materials. Traditional protocols for identifying mantle-equilibrated zircon require a comprehensive examination of whole rock geochemistry in addition to zircon morphology, texture, and trace element and isotopic measurements. This study proposes a simple filter scheme for selecting mantle-equilibrated zircon using trace element systematics alone (P, Ti, Y, Nb, rare earth elements [REE], Hf, Th, and U) to provide the geological context of zircon from three perspectives: (1) mineral inclusions; (2) source melt petrogenesis; and (3) zircon saturation context. The filter scheme presented here, comprising of 13 criteria, is established based on detailed classifications of 2,173 zircon analyses from 30 independent references and is shown to distinguish between nonmagmatic zircon, magmatic zircon with significant inclusions and/or sourced from highly enriched source melts, and mantle-equilibrated zircon. The filter scheme is validated with known, well-characterized mantle-equilibrated Jack Hills zircon ($n = 53$) and derives an average mantle redox state of ΔFMQ 1.5 ± 1.3 (sd) circa 4,400 Ma, in agreement with previously published results. Further application of the filter scheme to zircon dataset ($n = 76$) from three metasedimentary rocks successfully reveals the mantle-equilibrated zircon in the dataset, and implies a mantle redox state of ΔFMQ − 1.5 ± 1.3 (sd) circa 2,950 Ma. This filter scheme can be applied to studies of out-of-context detrital and/or xenocrystic zircon in the future.

Plain Language Summary Zircon is a robust accessory mineral commonly found in felsic rocks. The Ce/Ce* and Ti content in zircon can be used to infer the redox states of local magmatic environments from which they crystallized. Importantly, only mantle-equilibrated zircon (i.e., unaltered magmatic zircon that crystallized from melts without interaction to the hydrosphere nor assimilated exogenous materials) record the chemistry of mantle source, and provide insights of mantle redox state via zircon Ce/Ce* oxybarometry and Ti-in-zircon thermometry. Traditionally, the identification of mantle-equilibrated samples has relied on comprehensive examination of zircon and their host rocks (i.e., whole rock geochemistry, zircon morphology, texture, and trace element and isotopic measurements) in order to obtain information for zircon saturation context, source melt petrogenesis, and postmagmatic history. This study, however, presents a simple filter scheme that facilitates the selection of mantle-equilibrated zircon and provides insights about zircon petrogenesis using trace element systematics alone (P, Ti, Y, Nb, REE, Hf, Th, and U).

1. Introduction

Magmatic oxygen fugacity (or fO_2) is an important control on elemental behavior, such as solubility (e.g., soluble Fe^{2+} vs. insoluble Fe^{3+}), mobility (e.g., mobile UO_4^{+} vs. immobile U^{4+}), chemical affinity (e.g., siderophile S at low fO_2 vs. lithophile S at high fO_2), and compatibility (e.g., compatible Eu^{2+} vs. incompatible Eu^{3+} in plagioclase). Understanding the fO_2 of the upper mantle in the early Earth is particularly valuable for quantitatively describing processes associated with planetary differentiation (e.g., Frost & McCammon, 2008; Frost et al., 2008; Yang et al., 2014) and the evolution of atmospheric composition (e.g., Kump et al., 2001; Lee et al., 2014; Trail et al., 2011).

Zircon ($ZrSiO_4$) is a resilient accessory mineral capable of surviving multiple igneous or metamorphic events, weathering and transport, hydrothermal alteration, etc. In the zircon crystal lattice, $VIIIZr^{4+}$ may be exchanged for a range of incompatible trace elements, which provides valuable insights about the local

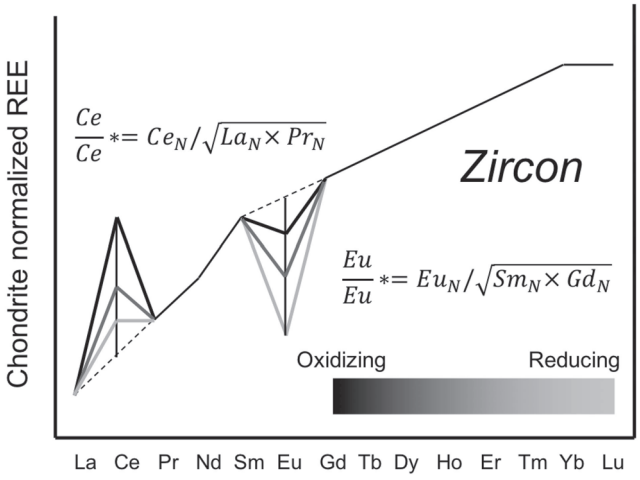

Figure 1. Schematic chondrite normalized pattern of REE in zircon. Ce/Ce* and Eu/Eu* are calculated as $Ce_N / \sqrt{La_N \times Pr_N}$ and $Eu_N / \sqrt{Sm_N \times Gd_N}$ respectively, where the subscript *N* indicates trace element values normalized to CI chondrites (McDonough & Sun, 1995). As the oxygen fugacity of the system increases (darker shade of gray), Ce/Ce* is expected to increase whereas Eu/Eu* is expected to decrease. The majority of terrestrial magmatic zircon have both positive Ce/Ce* and negative Eu/Eu*.

magmatic environment from which it crystallized. For example, studies of zircon chemistry have been used to infer: melt crystallization temperatures based on Ti concentrations in zircon (e.g., Ferry & Watson, 2007; Siégel et al., 2018; Watson & Harrison, 2005); the timing of crystallization and/or metamorphism from U–Pb radiometric dating (e.g., Tichomirowa et al., 2013; Zheng et al., 2004); the provenance of source material from concentrations of large ion lithophile elements and high-field strength elements (HFSEs; e.g., Belousova et al., 2002; Chapman et al., 2016; Grimes et al., 2007, 2015; Hoskin & Ireland, 2000); and the degree of crustal assimilation in magmatic systems based on coupled O-Hf isotopes (e.g., Hawkesworth & Kemp, 2006; Page et al., 2007; Spencer et al., 2017; Trail et al., 2007).

Of particular importance, magmatic fO_2 has been inferred from the abundances of multivalent elements, namely Ce (3+, 4+) and Eu (2+, 3+), relative to other monovalent rare earth elements (REE; 3+ only). In zircon, REE^{3+} can replace Zr^{4+} in a coupled substitution with additional cations (e.g., P^{5+}) to balance charge. The compatibilities of trivalent REE in zircon increase systematically from La to Lu due to progressively smaller ionic radii with increasing atomic number (commonly termed the lanthanide contraction; Figure 1).

Under oxidizing conditions, a greater proportion of Ce is present as the higher Ce^{4+} valence state, resulting in preferential incorporation into the zircon structure (relative to Ce^{3+}) due to its smaller ionic size and equivalent charge to Zr^{4+}. This substitution bias results in an enrichment of Ce relative to nearby trivalent elements La and Pr in normalized composition diagrams, enabling the quantification of a Ce anomaly as: $Ce/Ce^* = Ce_N / \sqrt{La_N \times Pr_N}$. In comparison, under reducing conditions, a greater proportion of Eu takes on the lower Eu^{2+} valence state. Because Eu^{2+} is too large to fit into the zircon structure without incurring significant lattice strain, Eu shows a depletion relative to neighboring trivalent Sm and Gd, defining a Eu anomaly as: $Eu/Eu^* = Eu_N / \sqrt{Sm_N \times Gd_N}$. As a compounding effect, the fractionation of plagioclase also contributes to Eu/Eu* in zircon because Eu^{2+} is highly compatible in the plagioclase structure. Consequently, Ce/Ce* (and to a lesser extent Eu/Eu*) in magmatic zircon can be used as a proxy for magmatic fO_2.

1.1. Quantitative Zircon Ce/Ce* Oxybarometry and Ti-in-Zircon Thermometry

The Ce/Ce* recorded in zircon has been experimentally calibrated to fO_2 of silicate melts at various alumina and water concentrations (Burnham & Berry, 2012; Loucks et al., 2020; Smythe & Brenan, 2015, 2016; Trail et al., 2011, 2012). However, statistically, the majority of natural zircon crystallizes in hydrous alumina-saturated melts (i.e., determined by the molar ratio of $Al_2O_3/(Na_2O + K_2O)$, or A/NK > 1) at relatively lower temperatures (e.g., ~800°C). Therefore, the empirical relationship that most universally describes Ce partitioning behavior in natural zircon is summarized by Trail et al. (2012),

$$\ln\left(\frac{Ce}{Ce^*}\right) = \left(0.1156 \pm 0.0050\right) \times \ln\left(fO_2\right) + \frac{13860 \pm 708}{T(K)} - \left(6.125 \pm 0.484\right) \quad (1)$$

where the experiments were conducted at 10 kbar and 800–1,300°C with 2–10 wt% H_2O.

The zircon crystallization temperature *T* in Equation 1 can be inferred from the Ti concentration in zircon following the quantitative relationship (Ferry & Watson, 2007):

$$\log\left(\text{Ti in zircon ppm}\right) = \left(5.711 \pm 0.072\right) - \frac{4800 \pm 86}{T(K)} - \log\left(a_{SiO_2}\right) + \log\left(a_{TiO_2}\right) \quad (2)$$

The activities of SiO_2 $\left(a_{SiO_2}\right)$ and TiO_2 $\left(a_{TiO_2}\right)$ are dimensionless quantities that describe the chemical potentials of SiO_2 and TiO_2 of the system relative to quartz and rutile, respectively.

Ce/Ce* oxybarometry and Ti-in-zircon thermometry are often applied together to provide a streamlined estimation of magmatic fO_2. This value is reported as orders of magnitude deviations from the fO_2 of the mineral assemblage fayalite-magnetite-quartz (FMQ) at a specific temperature (or ΔFMQ) to infer the melt redox state of local magmatic environment (Chou, 1978).

1.2. Challenges at Selecting Mantle-Equilibrated Zircon

Melt redox states that inferred from mantle-equilibrated zircon provide valuable insights into mantle redox conditions. Mantle-equilibrated zircon refer to unaltered magmatic zircon derived from source melts that have not interacted with the hydrosphere nor assimilated exogenous materials (e.g., sediments and crustal materials). However, the mantle-equilibrium state may be violated by a host of geological processes, which are summarized into three main categories: (1) mixing of melt from multiple sources (e.g., genetically distinct mantle magmas, assimilated crustal rock, etc.); (2) dynamic growth conditions (e.g., disequilibrium crystallization, mineral decomposition during metamorphism, etc.); and/or (3) modification of zircon trace element concentrations via postmagmatic processes (e.g., subsolidus crystallization, hydrothermal alteration, etc.). These processes diversify the composition of the source melts, and change trace element signatures syn- and/or post-zircon saturation, resulting in an unrealistic spread in inferred melt redox states that extend below conditions expected at the core mantle boundary (ΔFMQ < −4; McCammon, 2005) to those found in the modern atmosphere (ΔFMQ > +10; McCammon, 2005). Therefore, selection of mantle-equilibrated zircon is necessary to obtain meaningful mantle oxygen fugacity.

Evaluation of zircon mantle-equilibration state traditionally requires a number of analytical protocols including (but not limited to):

1. Determination of whole rock chemistry to estimate the source melt compositions, calculate an apparent zircon/melt partition coefficient for Ce, infer the crystallization behavior (equilibrium vs. disequilibrium), and growth environment of zircon.
2. Petrographic examination and/or chemical mapping (e.g., via back-scattered electron [BSE] or cathodoluminescence [CL] imaging) to characterize zircon morphology and texture, identify mineral or fluid inclusions, evaluate intragranular and intergranular chemical and isotopic variation based on zoning, and infer petrogenetic history (Corfu et al., 2003; reference therein).
3. Isotopic measurements in individual zircon crystals; for example, U–Pb radiometric dating to understand the age populations of zircon in host rocks, and oxygen isotopes to gauge the degrees of interaction to the hydrosphere in source melts of zircon.
4. Chemical filtering to exclude zircon that carry trace element signatures indicative of mineral inclusions (e.g., apatite, etc.; Bell et al., 2019) and nonmagmatic features (i.e., hydrothermal and metamorphic zircon; Hoskin & Black, 2002; Hoskin, 2005).

These requirements are highly recommended to obtain a thorough understanding of zircon saturation conditions, constrain statistical variances, and add confidence to the inferred melt redox states. For instance, the application of these methods has enabled the demonstration that mantle-equilibrated zircon center around the FMQ buffer (e.g., Trail et al., 2011). However, such strict protocols also reduce the size of viable datasets and ultimately undermine the capability/advantage of the method by requiring extensive analyses that may not be feasible given financial (cost), programmatic (time), and/or logistical (sample volume/size) limitations. For example, considering the small size of a zircon grain, plus the challenges associated with avoiding areas where clear inclusions or fractures are identified, it is often difficult to ablate sufficient sample volume of zircon for replicate analyses.

1.3. Purpose of This Study

The purpose of this study is to establish a multidimensional filter scheme that facilitates the selection of mantle-equilibrated zircon based on a narrow range of trace element systematics. Instead of relying on

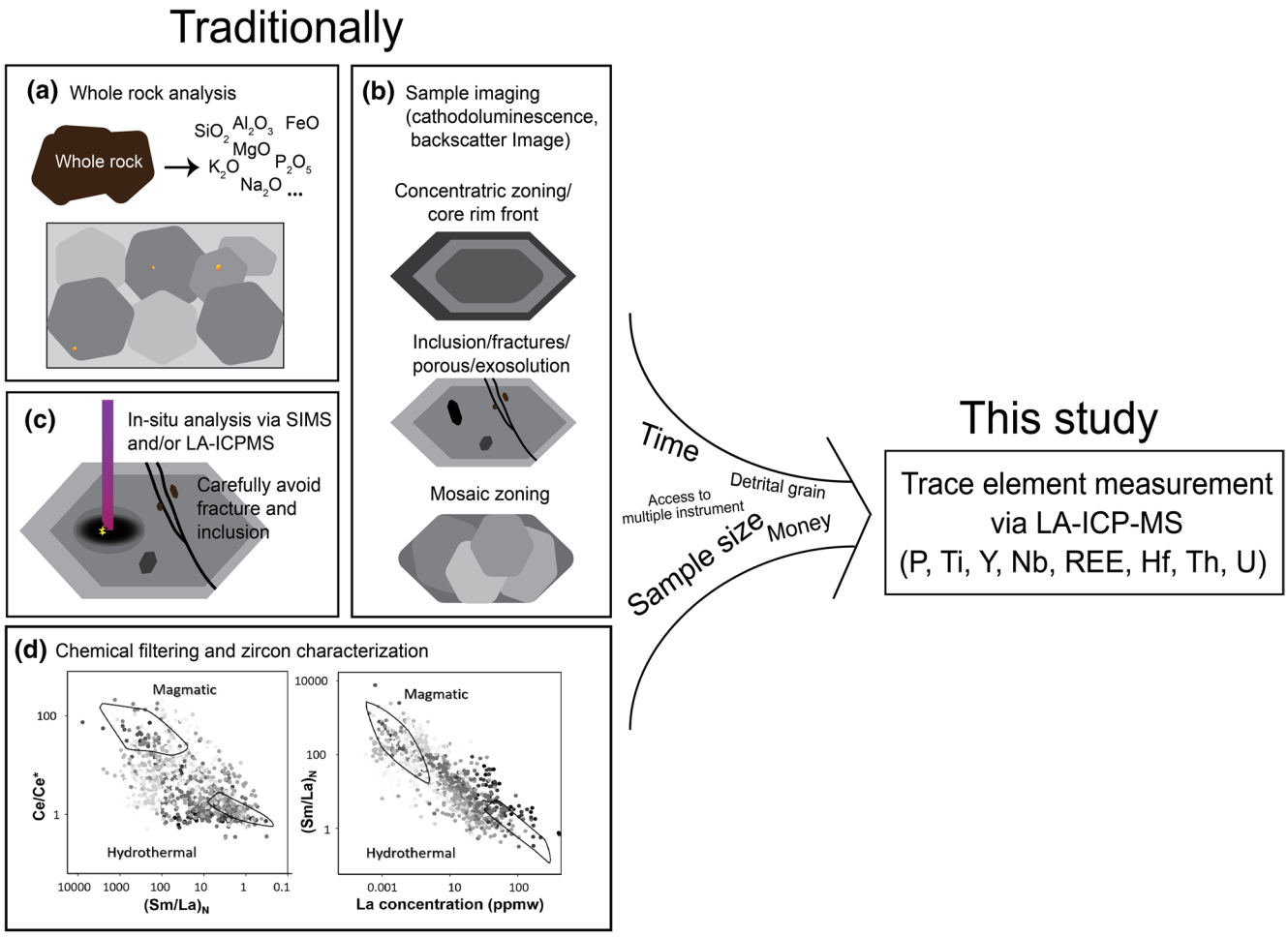

Figure 2. A comparison diagram between traditional approaches to screening for mantle-equilibrated zircon, and the filtering criteria pioneered in this study.

extensive contextual observations (e.g., petrography, whole rock compositions, and oxygen isotope ratios), trace element abundances and dynamics are used to isolate zircon that have experienced diverse geological processes (e.g., inclusions, sub-solidus crystallization, crystallized from melt with potential interaction to hydrosphere, etc.), so that the combined filters can screen effectively for mantle-equilibrated zircon (Figure 2). These chemical criteria are first justified based on previously published reviews, experiments, and simulation, and then evaluated objectively by applying the methods developed here to robust, publicly available zircon datasets. Zircon with the greatest compositional similarity to the canonical trace element chemistry of mantle-equilibrated zircon should theoretically have the highest probability of recording and preserving the signature of the local mantle redox states.

2. Zircon Data Compilation and Preparation

In order to establish, validate, and demonstrate the filter scheme proposed here, this study compiled and prepared three separate zircon datasets, which correlate to Sections 5.1–5.3 respectively.

2.1. Establishment of a Multidimensional Filter Scheme

The establishment of the filter scheme relies on the exploitation of trace element criteria that effectively constrain the saturation condition of zircon. Though each individual criterion used here is summarized from previously published review studies and/or justified with experiments and simulation, we also compiled a zircon dataset from 30 independent references with the following trace element measurements: P,

Ti, Y, Nb, REE, Hf, Th, and U (see Supporting Information I) to statistically evaluate the efficacy of each trace element proxy. Zircon entries without trace element concentrations listed, or with concentrations below detection limits, are not used in this study. In the end, the dataset contains 2,173 individual zircon analyses from a wide age distribution (i.e., Mesozoic to Archean zircon) and range of tectono-environments (e.g., continental/island arc, postcollisional boundary, intraplate ocean island, etc.). Each entry is labeled with host rock type (i.e., igneous, metamorphic, detrital, carbonatite, kimberlite, and mineral deposits) and zircon description from BSE and CL imaging (i.e., magmatic, magmatic with inclusion, magmatic with metamorphic rims, magmatic with hydrothermal rims, metamorphic, hydrothermal, and metamict). The classification is left blank if no host rock or contextual information is provided in the literatures. Such detailed labeling facilitates the selection of individual trace element criterion in Section 3, and helps to propose and establish the multidimensional filter scheme in Sections 4 and 5.1.

2.2. Validation of Filter Scheme With Jack Hills Zircon

We validate the filter scheme by interrogating a Jack Hills zircon dataset (see Supporting Information I). The zircon in this dataset have been characterized previously via BSE/CL imaging, oxygen isotope analyses, U–Pb age determinations, and trace element measurements by Cavosie et al. (2006); the Ti content of each zircon was reported by Fu et al. (2008). This validation dataset contains 53 zircons in total, though some samples are missing specific chemical information (e.g., Nb content and some age and oxygen isotope measurements). The same dataset has been used to estimate the oxygen fugacity of Hadean magmas in Trail et al. (2011). Therefore, a direct comparison of our selected zircon and inferred melt redox states to previous studies enables a critical test of the performance of the proposed filtering scheme here.

2.3. Case Study: Application of Filter Scheme to a Zircon Dataset from Greenland

We further apply this filter scheme to a zircon dataset ($n = 76$) from three metasedimentary rocks 524994, 524906, 524907 that sampled at Kangerdluarssuk Fjord, southern West Greenland. Sample 524906 and 524907 have been published in Dyck et al. (2015). The trace element measurements of three samples, including U–Pb dating, were collected using the same methods via LA-ICP-MS (see Supporting Information II or Dyck et al., 2015 for details). This case study has a full set of trace element measurements (see Supporting Information I), and is meant to demonstrate the application of this filter scheme at facilitating zircon research.

2.4. Estimates and Uncertainty of Ti-in-Zircon Temperature and Inferred Magmatic fO_2

The Ce/Ce*, Ti-in-zircon temperatures, and melt redox states of all zircon entries in three datasets were calculated using Equations 1 and 2. The values of variables a_{SiO_2} and a_{TiO_2} were approximated according to the following arguments. In the literatures, a_{SiO_2} is usually assumed to be unity as zircon most commonly crystallize from melt that is close to quartz saturation (Ferry & Watson, 2007). The value of a_{TiO_2} in silicic melts at appropriate magmatic temperature is typically between 0.6 and 1, and it can be estimated based on the crystallization of mineral phases at equilibrium with zircon, such as rutile ($a_{TiO_2} = 1$), and ilmenite and/or titanite ($a_{TiO_2} = 0.6$; Ferry & Watson, 2007; Watson et al., 2006). In applications to quartz-free crustal rocks and/or detrital zircon with limited or no geological context, the uncertainty in a_{SiO_2} and a_{TiO_2} will impose only limited effects on calculated temperatures. For example, assuming $a_{SiO_2} = 1$ and $a_{TiO_2} = 1$ yields an uncertainty up to 70°C at 750°C (Ferry & Watson, 2007). Therefore, for simplicity, this study calculates Ti-in-zircon temperatures and derives inferred melt redox states assuming a_{SiO_2} and a_{TiO_2} of unity. However, when justification of a_{SiO_2} and a_{TiO_2} is available, accurate a_{SiO_2} and a_{TiO_2} values are highly recommended to reduce the uncertainty of inferred melt redox state. By comparing the melt redox states determined from this study to previously published values (see Section 5.2), the external reproducibility of magmatic fO_2 calculations is estimated to be 1.3 log units at one standard deviation (sd) for mantle-equilibrated zircon.

3. Justification of Independent Criteria Used to Constrain Zircon Source Chemistry/Dynamics

As mentioned in Section 1.2, the variance of inferred melt redox states derived from Ce/Ce* and Ti content in zircon can be artificially modified by geological processes from three categories: (1) mineral inclusions, (2) source melt petrogenesis, and (3) saturation context of zircon. The trace element systematics of zircon associated with these processes have been explored independently in previous studies via simulations, experiments, and global datasets, which are summarized below as foundations for selecting filtering criteria.

3.1. Mineral Inclusions in Zircon

Mineral inclusions are common in igneous zircon. Some inclusions act as nucleation sites for crystallizing zircon crystals in melt (i.e., primary inclusions); others, however, are alteration or exsolution features reflecting hydrothermal and/or metamorphic activity (i.e., secondary inclusions). The scale of such intragranular heterogeneity varies from visible micron-sized inclusions to nanoscale trace element enrichment zones (Anderson et al., 2008; Bell et al., 2015; Corfu et al., 2003; Hofmann et al., 2014). Therefore, sampling of inclusion phases and/or local enrichment zones cannot be completely avoided even with high-resolution petrographic imaging. Spatially resolved analytical techniques that characterize exceedingly small sample volumes (e.g., secondary ion mass spectrometry) are particularly susceptible to disproportionate sampling of trace amounts of inclusions or nanoscale enrichments.

Based on this study, measurements of zircon plagued by primary and secondary inclusions can lead to 15 orders of magnitude variation in inferred melt redox states, as such phases may inflate estimates of Ti-in-zircon temperature (e.g., via excess Ti derived from titanite and magnetite) and/or attenuate the magnitude of observed Ce/Ce* anomalies (e.g., via overprinting REE signatures). Simple two-component mixing between a variety of phases commonly included in zircon (i.e., apatite, titanite, allanite, xenotime, and monazite) and the most primitive zircon grain from the case study reviewed in Section 5.3 demonstrates that as little as 0.0001 wt% of monazite and allanite inclusions will reduce Ce/Ce* by more than 80%. Interestingly, 0.5 wt% of inclusions enriched in light REE (LREE) will overprint the Ce/Ce* signature completely (Figure 3), in agreement with the results from previous study (Zhong et al., 2018b).

Therefore, due to the high sensitivity of Ce/Ce* oxybarometry to mineral inclusions and the potential risks of sampling them, selecting inclusion-free magmatic zircon is one of the most important steps for limiting artificial variances in inferred melt redox states.

Historical criteria for filtering hydrothermal zircon include Ce/Ce*, La concentration, $(Sm/La)_N$, and LREE index (LREE_I), calculated as the concentrations of Dy/Nd + Dy/Sm (Bell et al., 2019; Hoskins 2005). Based on petrographically predetermined magmatic and hydrothermal zircon, filtering schemes previously proposed in literatures targeting the selection of unaltered magmatic zircon are Ce/Ce* $\leq$ 100, La between 0.002 and 0.5 ppmw, $(Sm/La)_N$ between 30 and 1,000, and LREE_I > 60. Because Ce/Ce* is one of the input parameters for calculating oxygen fugacity via Equation 1, the range of Ce/Ce* is especially important for accurately determining melt redox states. The traditional upper boundary Ce/Ce* $\leq$ 100 is adopted as a filter for magmatic zircon, because zircon with Ce/Ce* > 100 can be inferred to an unrealistic magmatic environment as oxidized as modern atmosphere (ΔFMQ > +10; McCammon, 2005) at the most probable zircon saturation temperature. The lower boundary of Ce/Ce*, however, cannot be directly inferred because it varies with the amount of REE in the melt, as well as the mixing ratio of inclusions in the sample. Therefore, instead of setting a lower boundary of Ce/Ce*, the other three parameters, La concentration, $(Sm/La)_N$, and LREE_I, are used to elucidate the fraction of inclusions within zircon.

Figure 4 shows the sensitivity of La concentration, $(Sm/La)_N$, and LREE_I for filtering mineral inclusions of different mixing ratios to zircon. La < 0.1 ppmw is the most sensitive parameter that is able to filter out zircon with mineral inclusions as low as 0.0001 wt%, but such sensitivity is reduced by up to three orders of magnitude if the traditional upper boundary of La concentration (La < 0.5 ppmw) is used instead. Similarly, $(Sm/La)_N$ > 100 is able to discern 0.0001 wt% monazite and allanite, but relaxing the requirement

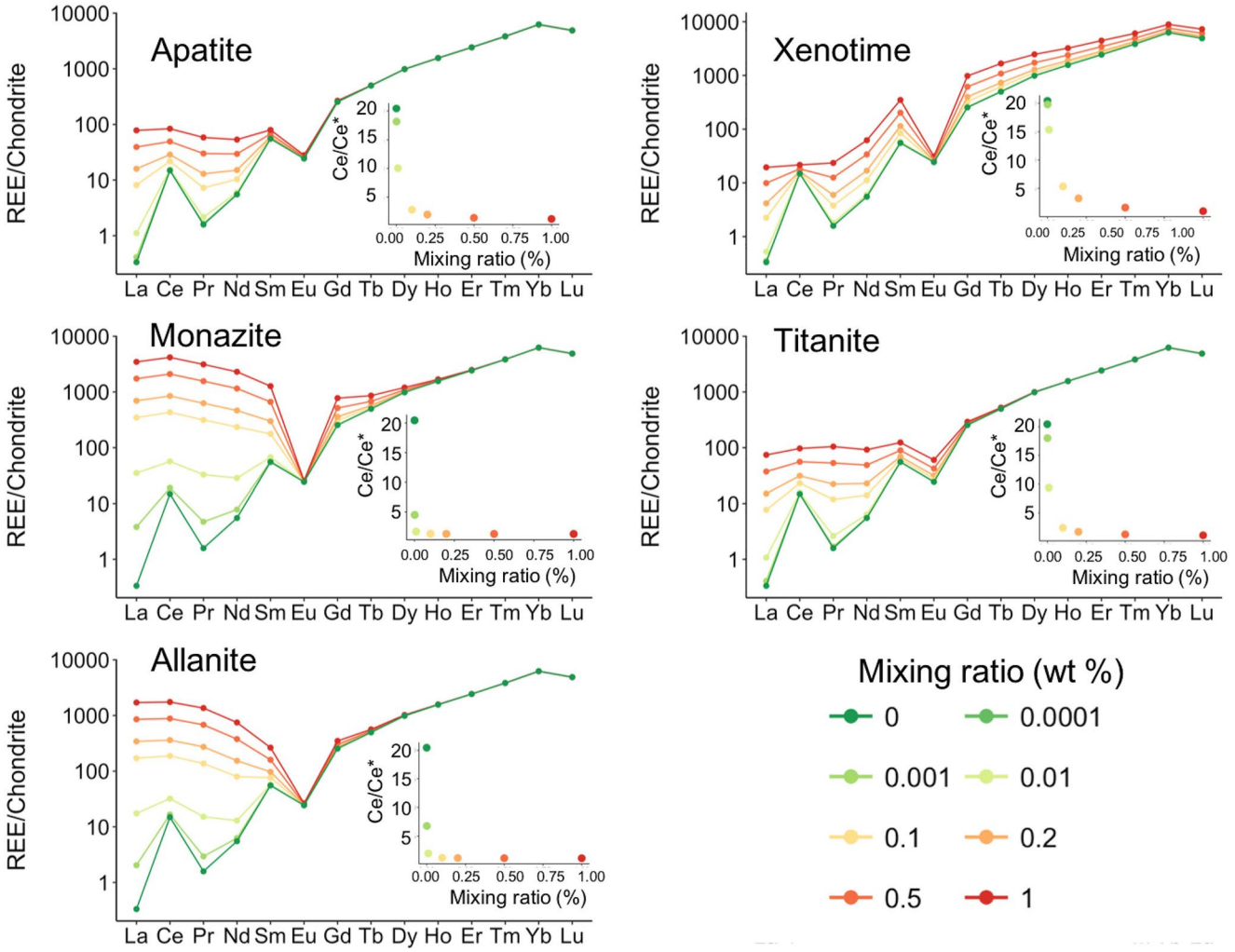

Figure 3. Mixing models between zircon and potential inclusions across a range of mixing proportions demonstrate the sensitivity of Ce/Ce* to chemical overprinting. The REE concentration of unadulterated zircon is modeled after sample 524994 Zircon 76, the most primitive zircon grain from the case study reviewed in Section 5.3. The average REE concentration of apatite is from Zhong et al. (2018a), and the compositions of the other phases (xenotime, monazite, titanite, and allanite) are from Bea et al. (1996) (see Supporting Information I). The insets describe the relationship between Ce/Ce* and the mixing ratios of inclusions.

to traditional selection value $(Sm/La)_N > 30$ masks up to 0.2 wt% of xenotime, which can attenuate Ce/Ce* by 80%. Although LREE_I is the least sensitive parameter among these three, it is important to use an additional LREE-independent criterion to monitor inclusions because the LREE measurements in zircon are analytically challenging due to their low absolute abundances. Further, because trace element concentrations of each mineral inclusion vary over two orders of magnitudes in natural samples, multidimensional criteria can increase the filtering power and reduce the probability of detecting inclusions. Other LREE-independent criteria commonly used to detect inclusions in zircon include Ca and Fe contents, as elevated abundances of these elements commonly reflect apatite and magnetite inclusions respectively (Bell et al., 2019). However, these proxies are found to be less sensitive at identifying inclusions than LREE-dependent criteria using the zircon dataset from Bell et al. (2019), thus La concentration and $(Sm/La)_N$ are preferred in this study.

In summary, the boundaries of historical filtering criteria are updated. The current filtering schemes define samples with the highest probabilities of reflecting unaltered mantle-equilibrated zircon: La concentration between 0.1 and 0.002 ppmw, $(Sm/La)_N$ between 100 and 1,000, and LREE_I > 60. In addition, Ce/Ce* ≤ 100 is adopted to distinguish magmatic zircon.

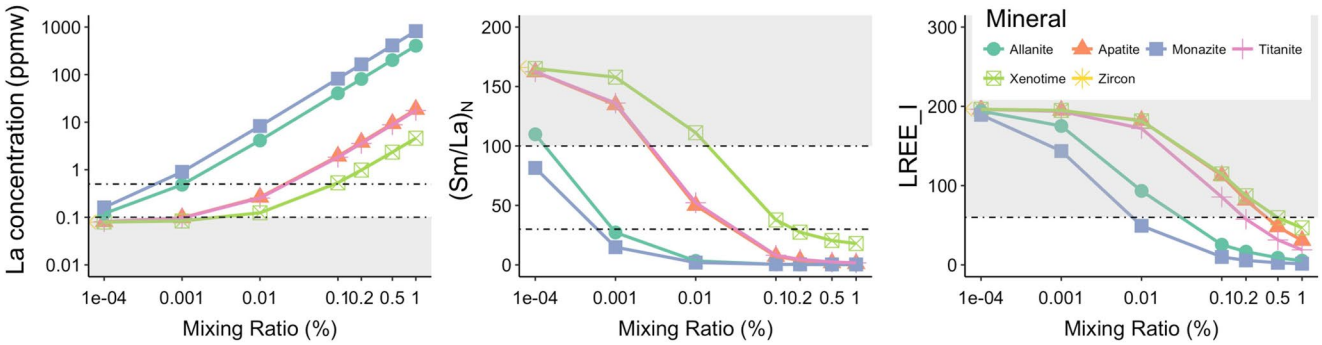

Figure 4. A sensitivity comparison between all three inclusion indicators: La concentration, $(Sm/La)_N$, and LREE_I as a function of mixing ratios (%). The shaded areas represent regions that will be accepted by the filter scheme.

3.2. Source Melt Petrogenesis

Zircon starts to crystallize when the Zr availability in the source melt is greater than or equal to the zircon saturation content. Zircon saturation content, or the minimum Zr concentration required to precipitate zircon in the melt, tends to decrease with an increasing degrees of melt polymerization and/or decreasing magma temperature (Boehnke et al., 2013; Hanchar & Watson, 2003). For example, the zircon saturation content in basaltic magma is about 2,000–30,000 ppmw Zr (Shao et al., 2019) but reduces to ~100 ppmw in silicic magma (Watson, 1979). The availability of Zr in the melt, however, is constrained and remains relatively constant; for example, the average Zr content in global Mid Ocean Ridge Basalt (MORB; ~100 ppmw Zr; e.g., Arevalo & McDonough, 2010) is similar to the composition of the bulk continental crust (~130 ppmw Zr; e.g., Rudnick, 1995). Despite similar Zr availability, the zircon saturation contents of these two systems are dramatically different because melt polymerization serves as a dominant control, and prevents the crystallization of zircon in mantle-derived magma unless the source melt interacts with metasomatic fluids or assimilates exogenous materials (e.g., marine sediments, slab-derived melt, or crusts). In fact, the source melts of most zircon in ultramafic and/or mafic host rocks in compiled datasets are interpreted as melt products of metasomatized mantle-wedge, or contaminated mantle-derived melt that mixed with slab-derived fluids or crustal materials during ascent (e.g., Janoušek et al., 2019; Robinson et al., 2015; Tichomirowa et al., 2013; Sun et al., 2018; Vilalva et al., 2019, etc.). Because fluids and surface materials have undergone various low temperature processes (chemical and mechanical weathering, erosion, etc.) and commonly possess enriched incompatible trace element abundances, assimilation of these materials can easily overprint the inherited fO_2 signatures from the original mantle source. Therefore, in this study, we employ two trace element proxies to infer the generation of the source melts, and to gauge the interactions of source melts to metasomatic fluids and surface materials.

3.2.1. Source Melts From Igneous Sources: $P \leq 750$ ppmw and $(REE + Y)/P$ Molar Ratio > 1

Zircon commonly crystallize in granitic melts, which can derive from both igneous sources (I-type granite, alumina-saturated metaluminous melt) and sedimentary sources (S-type granite, alumina-oversaturated peraluminous melt). Generation of melts from a sedimentary protolith implies little to nothing about mantle redox conditions, so zircon from S-type granitoids provide less insight into the deep Earth compared to mantle-equilibrated zircon.

Zircon phosphorous (P) concentration provides a gauge to identify the type of granitic protolith. The average P concentration of global MORB is ~600 ppmw (Arevalo & McDonough, 2010). Due to its incompatibility to most major minerals, the P concentration of a melt may increase as the magma differentiates until apatite precipitates. Apatite ($Ca_5(PO_4)_3(OH, Cl, F)$) is a common accessory phase that crystallizes prior to zircon saturation in metaluminous melt (Lee et al., 2014), but dissolves in peraluminous melt as magmatic differentiation continues (Mysen et al., 1997). Despite the insignificant difference of bulk rock P_2O_5 concentration between S-type and I-type granites, the saturation and dissolution of apatite control the availability of P in residual melts.

In general, S-type zircon inherit a higher P concentration, whereas only 10% of I-type zircon have P concentration > 750 ppm (Burnham & Berry, 2017). Moreover, S-type zircon is observed to have a strong linear correlation between the molar ratios of REE + Y and P, whereas I-type zircon are observed to have (REE + Y)/P molar ratio > 1. This is because coupled substitution between P^{5+} and $(REE, Y)^{3+}$ for Zr^{4+} becomes dominant in melt with a higher P concentration. The lack of linear correlation in I-type zircon implies preference of additional REE incorporation mechanisms in P-deficient metaluminous melt. In a case study by Burnham and Berry (2017), the authors suggest that the combined criteria P ≤ 750 ppm and (REE + Y)/P molar ratio > 1 enables the isolation 96% of I-type zircon based on 144 zircon analyses from characterized S-type and I-type granites; thus, we adopt these values here.

Similar source melt information has been inferred from Eu/Eu* (Wang et al., 2012, see Section 3.3.4) and Al content in detrital zircon (Trail et al., 2017). Although they are not specifically addressed in these sections, they could be considered as alternative criteria for differentiating source melts.

3.2.2. Limited Interaction With Fluids and Surface Materials: U/Nb ≤ 20 and/or Th/Nb ≤ 10

Partial melting of basaltic systems, especially at arc settings, often involves fluid components and/or surface materials (e.g., marine sediments and continental crust). The degree of such interaction can be inferred from U/Nb, Th/Nb ratios in zircon. Fluid immobile Nb fractionates from fluid mobile Th and U during low temperature surface weathering, erosion, and fluid interaction. Thus, normalization of Th and U to Nb can be used as a monitor for mixing with such exogenous materials.

Based on over 5,300 zircon analyses compiled by Grimes et al. (2015), zircon formed in arc magmas may be distinguished from those derived from mid-ocean ridges and intraplate ocean islands by notably higher U/Nb > 20 and Th/Nb > 10. These chemical signatures can be explained by the assimilation of Th- and U-enriched sediments, or due to incorporation of fluid mobile Th and U into resultant magma during metamorphic dehydration of the subducted crusts. Therefore, zircon with U/Nb ≤ 20 and/or Th/Nb ≤ 10 best represent crystallization from mantle-equilibrated melt without sufficient exchange with fluids and surface materials.

Similar trace element systematics for assessing zircon with limited fluid interaction and surface material assimilation include U/Yb and Th/Yb (Grimes et al., 2007, 2015). However, the specific values of these ratios vary if source melt originates from variably enriched mantle sources. For example, while low U/Yb (< ~0.1) appears to be diagnostic of zircon from differentiated melt originating from a depleted mantle source, zircon from relatively enriched geochemical reservoirs typically carry higher U/Yb ratios (Carley et al., 2014; Grimes et al., 2007, 2015). Normalization of U/Yb and Th/Yb to Nb/Yb helps to reduce such effects, making U/Nb and Th/Nb preferred proxies in this study. However, when Nb measurements are not available (such as in Section 5.2), U/Yb and Th/Yb can be used as alternatives. For example, U/Yb ≤ 0.5 and Th/Yb ≤ 0.2 are recommended to distinguish zircon derived from mid-ocean ridges or intraplate ocean islands versus those sources from arc settings (e.g., Grimes et al., 2015).

3.3. Zircon Saturation Context

As a magma progressively differentiates prior to zircon saturation, the precipitation of major mineral phases will continuously change the availability of major elements in the melt, including redox-sensitive ratios such as Fe^{2+}/Fe^{3+}, thereby manipulating the local melt redox state. Saturation and/or dissolution of accessory phases, such as monazite or xenotime, can control trace element budgets in residual melts, thus changing the REE signatures inherited by zircon. In addition, the speed of magma differentiation and oversaturation of trace elements can lead to disequilibrium crystallization of zircon, resulting in observed partitioning behavior that deviate from calibrated relationships (e.g., Equation 1). Such magmatic processes play significant roles in changing local melt redox states and influencing trace element concentrations in zircon. Beyond saturation from magmatic melt, zircon can also experience re-equilibration, dissolution, and recrystallization in Zr-rich melts that source from the decomposition of Zr-rich mineral phases, or Zr-rich metasomatic fluids. In such cases, saturation of nonmagmatic zircon will not appropriately record the melt redox state via Equation 1.

We, therefore, employ five chemical filters to monitor for: (1) fractionation of redox-sensitive mineral phases and REE-enriched accessory phases; (2) degree of magma differentiation; (3) equilibrium crystallization of zircon; and (4) nonmagmatic zircon signatures.

3.3.1. Absence of Flat HREE Pattern: $(Lu/Gd)_N$ Between 10 and 74

The flat heavy REE (HREE) pattern observed in zircon could be due to the fractionation of garnet prior to or contemporaneous with zircon crystallization. Garnet is a redox sensitive mineral; the fractionation of garnet can alter the melt redox state by up to 6 orders of magnitude in arc settings (Tang et al., 2018), as Fe^{2+} is more compatible in garnet, leaving behind residual melt with a disproportionate concentration of Fe^{3+}. Because Fe serves as a major control on the local fO_2, an increase in $Fe^{3+}/\sum Fe$ in the residual melt (as promoted by fractionation of garnet) could effectively oxidize the system, consequently changing the Ce^{4+}/Ce^{3+} ratio in the melt relative to the original mantle setting. In addition, flat HREE patterns may also be imparted by metamorphic processes. Under high-temperature and high-pressure environments where garnet is stable, partial melting or decomposition of Zr-rich mineral phases (e.g., titanite) can contribute Zr, leading to subsolidus crystallization of zircon. Similarly, zircon in mantle-derived host rocks devoid of garnet (i.e., kimberlite and carbonatite) can also have flat HREE pattern due to incomplete melting of garnet in mantle source region (Hoskin & Schaltegger, 2003; Rubatto, 2017). As a result, zircon with flat HREE patterns often associate with the fractionation of garnet from melts, metamorphic origin of zircon, or disequilibrium crystallization in mantle-derived host rocks. Thus, we choose zircon without flat HREE patterns to imply local melt redox states.

Experimental results show that $D_{Lu}^{Zircon/Melt}$ / $D_{Gd}^{Zircon/Melt}$ in hydrous granitic melt is approximately 9 at 850°C and the ratio increases as magma cools (Rubatto & Hermann, 2007). The presence of garnet suppresses the partition of HREE into zircon; for example, $D_{Lu}^{Zircon/Garnet}$ / $D_{Gd}^{Zircon/Garnet}$ is 6 at 850°C, and further reduces to 1 as temperature increases to above 900°C (Rubatto & Hermann, 2007; Taylor et al., 2015). This agrees with empirical observations that mantle-derived zircon (in the presence of garnet) have $(Lu/Gd)_N$ ranging from 1 to 10, whereas metamorphic zircon cluster around $(Lu/Gd)_N$ approaching 1 (Kelly & Harley, 2005; Whitehouse & Platt, 2003), and typical granitic zircon have $(Lu/Gd)_N$ ranging from 16 to 74 (Hoskin & Schaltegger, 2003). Therefore, magmatic zircon without flat HREE patterns tend to have $(Lu/Gd)_N$ between 10 and 74.

3.3.2. Avoiding Fractionation of Accessory Phases: Th/U Ratio Between 0.2 and 4

Prior to or during zircon saturation, crystallization of Th-enriched phases (e.g., monazite and thorite) and/or U-enriched phases (e.g., coffinite, uraninite, or monazite) induces local heterogeneity of Th and U in the melt, enhancing observed Th/U variances in cogenetic magmatic zircon. Such heterogeneity can be further augmented via postmagmatic processes, such as hydrothermal alteration, metamorphism, and/or low temperature weathering. Hydrothermal fluids may mobilize, redistribute, or precipitate Th-rich and U-rich inclusions along cracks, or promote mass loss of U by oxidizing U^{4+} to form fluid mobile UO_4^{2-}. Metamorphism, decomposition, and crystallization of Th- and U-rich accessary phases can also incur spatial variations in Th and U concentration in melts, facilitating the dissolution and disequilibrium growth of zircon (Xiang et al., 2011). As a result, extreme values of Th/U in zircon can be used to imply significant fractionation of accessory phases from magma, disequilibrium crystallization, and nonmagmatic origin of zircon grains.

Based on 10,693 magmatic zircon analyses compiled in Kirkland et al. (2015), zircon Th/U ratios range from near 0 up to 19.8, with a median of 0.65 and a positive skewness of 6.7. Although metamorphic zircon exhibit a similar spread in Th/U, a greater percentage of metamorphic zircon have Th/U < 0.1 (Yakymchuk et al., 2018). Historically, Th/U < 0.1 was used as filtering tool for metamorphic zircon, but zircon in ultrahigh temperature metamorphic assemblage (>900°C) can also exhibit Th/U > 0.1, reinforcing the complexity of Th/U systematics (Kelly & Harley, 2005).

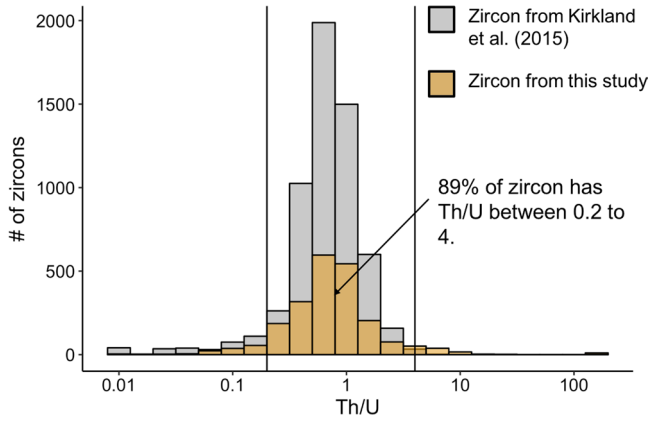

Figure 5. The distribution of Th/U in the compiled dataset (n = 2,173) from this study and magmatic zircon from Kirkland et al. (2015).

The large variance in Th/U recorded by natural zircon may be attributed to reasons mentioned above. However, the effects of each of these controls on Th/U ratios have not been fully deconvolved. Based on variation of zircon Th/U observed in compiled datasets from this study and from Kirkland et al. (2015), the Th/U of magmatic zircon is set to be within 0.2 and 4, which is about three times the interquartile range of compiled magmatic zircon dataset in Kirkland et al. (2015) and it includes 89% of compiled zircon analyses in this study (Figure 5).

3.3.3. Constraining Differentiation and Metasomatism: Hf Concentration: 5,000–14,000 ppmw

Zircon, as one of the primary carriers of Hf in magmatic systems, readily incorporate Hf into its crystal lattice due to the same valence state and similar ionic radius to Zr^{4+} (Wang et al., 2010). As HFSE, Hf and Zr are both highly incompatible in most mineral phases, so the Hf and Zr concentration in melt increases disproportionately with mineral fractionation, resulting an increasing Zr/Hf ratio in zircon as magma differentiates. Therefore, Hf concentration in zircon can be used to gauge the extent of magmatic differentiation.

According to 2,201 zircon electron microprobe analyses complied in Wang et al. (2010), Zr/Hf recorded by zircon in granites range from 5 to 100, showing a nearly normal distribution with a mean, median, and mode of 39. This mean Zr/Hf ratio is reproducibly observed among different studies of granitic zircon, but is notably higher than zircon from pegmatite or highly evolved rocks (i.e., Zr/Hf ratio ~20) (Claiborne et al., 2006; Linnen & Keppler, 2002; Pupin, 2000). Interactions with a fluid phase will reduce Zr/Hf ratio in zircon, resulting in an enrichment in Hf and a positive correlation between Hf and Rb (Linnen & Keppler, 2002). Conversely, the extreme high Zr/Hf ratio can be used as markers for fractionation of Hf-enriched accessary phases (e.g., hafnon) from magmatic system.

By assuming an average Zr concentration in zircon based on stoichiometry, a Zr/Hf ratio between 35 (the lower bound of granitic zircon; Claiborne et al., 2006) and 100 (the max value observed in the same dataset; Wang et al., 2010) equates to 5,000 to 14,000 ppmw Hf in magmatic zircon. Notably, zircon with Hf > 14,000 ppmw commonly exhibit higher La contents, corroborating a potential metasomatic influence and/or precipitation of LREE-enriched mineral phases (Claiborne et al., 2006). This compositional range overlaps with the Hf content observed in natural zircon (Claiborne et al., 2010) and includes approximately 88% of the data compiled in this study.

3.3.4. Equilibrated Crystallization of Zircon From Silicic Melt: Eu/Eu*: 0.1–0.6

Besides Ce, Eu is another REE that has two valence states, Eu^{2+} and Eu^{3+}. Eu^{2+} is strongly incompatible in the zircon structure due to its large ionic size and required coupled substitution in zircon structure, but Eu^{2+} is strongly compatible in the Ca^{2+} site in plagioclase. Therefore, fractionation of plagioclase depletes Eu in the melt. As a result, the Eu/Eu* ratios in zircon rarely exceed one, unless zircon saturates in disequilibrium conditions (Hoskin & Schaltegger, 2003; Trail et al., 2012).

The relationship between Eu/Eu* and Hf depicts a continuum of magma differentiation that connects zircon from mantle-derived melts (i.e., carbonatite and kimberlite) to silicic melt (i.e., igneous rocks; Figure 6). Majority of zircon in carbonatite and kimberlite are observed to have Eu/Eu* > 1, supporting the hypothesis that saturation of zircon in mantle-derived melt is thermodynamically unfavorable. However, as magma sufficiently evolves, zircon inherit a higher concentration of Hf and lower Eu/Eu*; for example, the majority of igneous zircon from this study have Eu/Eu* < 0.6 (Figure 6). The distribution of Eu/Eu* broadly correlates to types of parental magma. Zircon from S- and A-type granitoids have a distinctly lower Eu/Eu* < 0.1 than zircon from I-type granitoids (Sawaki et al., 2017; Wang et al., 2012). Therefore, mantle-equilibrated zircon are expected to have Eu/Eu* between 0.1 and 0.6.

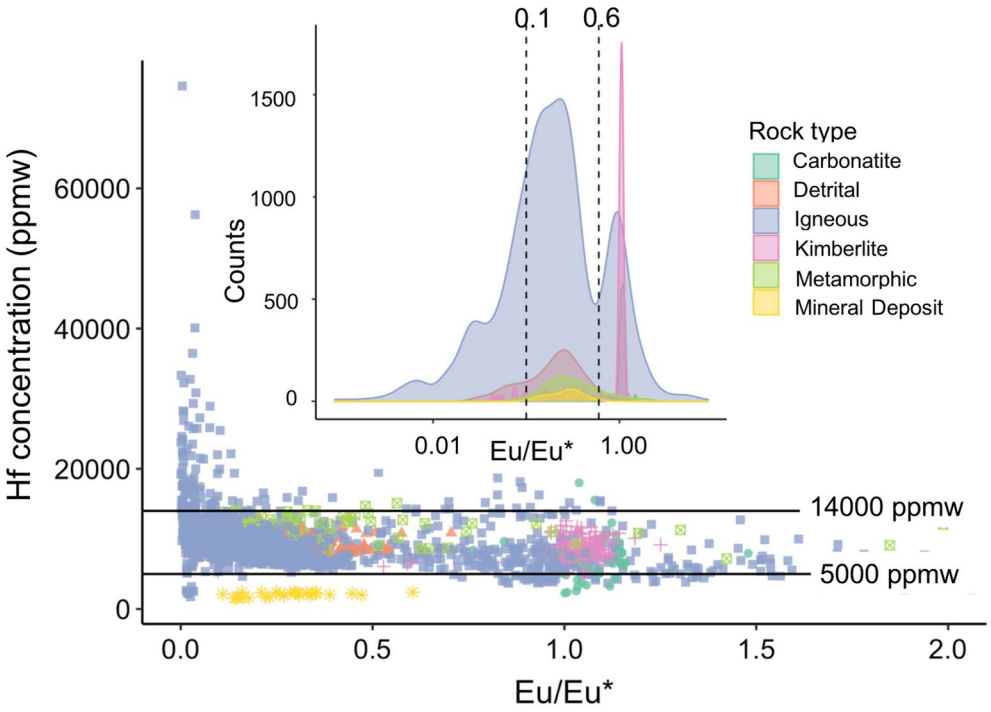

Figure 6. Hf concentration as a function of Eu/Eu* of zircon compiled in this study, categorized by host rock type. The inset shows the count distribution of Eu/Eu* of zircon by the type of host rocks. The count distribution is depicted by a kernel density estimation.

3.3.5. Saturation Temperature for Magmatic Zircon: Ti Concentration: 2–24 ppm

Titanium content in zircon is used to infer the zircon saturation temperature in magmatic systems (see Section 1.1). In a closed magmatic system, the onset of zircon saturation is controlled by the Zr availability versus the zircon saturation content in the melt as magma cools. By assuming a 100 ppmw initial Zr concentration in the system and a partition coefficient of $D_{Zr} \leq 0.01$ in the phases that first crystallize from a basaltic magma, zircon is expected to saturate starting at 850°C based on simulations of magma differentiation (Borisov, 2019; Lee et al., 2014; Nandedkar et al., 2014). This 850°C represents an upper bound, because the actual range of zircon saturation temperature is estimated to be ~ 800°C based on Ti systematics and the melt composition parameter M (i.e., the cation ratio of (Na + K + 2Ca)/(Al·Si) of the melt/whole rock) of 1,705 igneous zircon (Samperton et al., 2017; Siégel et al., 2018). Therefore, zircon saturating at temperature > 850°C likely reflect an open magmatic system subject to a disturbed trace element chemistry.

The majority of zircon data compiled in this study have Ti-in-zircon temperatures between 710°C and 810°C, consistent with the crystallization temperature range suggested by the simulations described above as well as literature values (Figure 7; Harrison et al., 2007; Fu et al., 2008). By assuming a_{SiO_2} and a_{TiO_2} unity in Ti-in-zircon thermometry, and considering the errors associated with Equation 2, we constrained the Ti concentration in magmatic zircon between 2 and 24 ppmw, corresponding to zircon saturation temperatures between 600°C and 850°C respectively. Zircon with Ti > 24 ppmw are indicative of zircon saturation from an open magmatic system at > 850°C, or an artificial enrichment of Ti content due to sampling of contamination phases, such as magnetite. The latter scenario can be effectively identified if a zircon fails mineral inclusion screening via La content, $(Sm/La)_N$, and LREE_I mentioned in Section 3.1.

4. Proposed Multidimensional Filter Scheme and Scoring System

Based on the discussion above, a total of 13 filtering criteria are summarized, all of which help to limit artificial variances in inferred melt redox states from three perspectives:

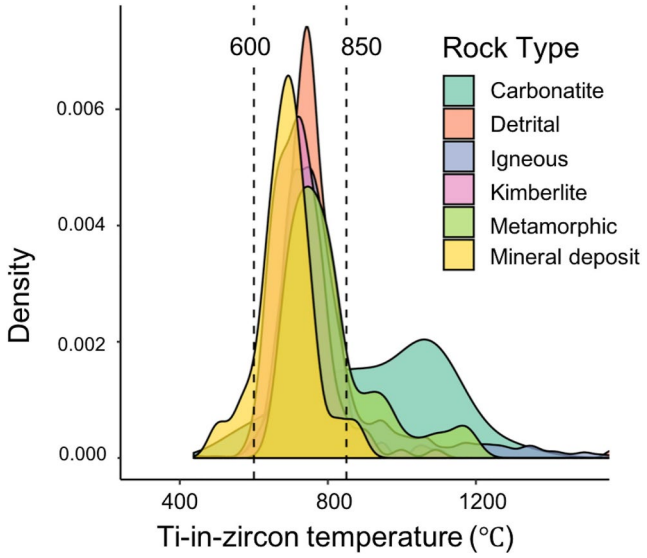

Figure 7. Density plot of Ti-in-zircon temperatures determined from the zircon dataset (n = 2,173) compiled here, categorized by the type of host rocks. The density plot uses a kernel density estimation and the area under each curve has a cumulative probability of 1.

		Y	N
Mineral inclusions	La: 0.002-0.1 ppmw	2	0
	$(Sm/La)_N$: 100 -1000	2	0
	LREE_I > 60	2	0
Source melt petrogenesis	U/Nb ≤ 20	1	0
	Th/Nb ≤ 10	1	0
	P ≤ 750 ppmw & (REE+Y)/P molar ratio > 1	1	0
Zircon saturation context	$(Lu/Gd)_N$: 10 to 74	1	0
	Hf: 5000 - 14000 ppmw	1	0
	Th/U: 0.2 - 4	1	0
	Eu/Eu*: 0.1 – 0.6	1	0
	Ce/Ce*≤ 100	1	0
	Ti: 2-24 ppmw	1	0
	Total score		**11**

Figure 8. An example of calculating the score of zircon that satisfy all criteria except that its U/Nb > 20, La concentration > 0.1 ppmw, and $(Lu/Gd)_N$ < 10.

1. Mineral inclusions in zircon:
   La concentration: 0.002–0.1 ppmw
   $(Sm/La)_N$ between 100 and 1,000
   LREE_I > 60
2. Source melt petrogenesis:
   U/Nb ≤ 20
   Th/Nb ≤ 10
   P ≤ 750 ppmw and (REE + Y)/P molar ratio > 1
3. Zircon saturation context:
   Ce/Ce* ≤ 100
   $(Lu/Gd)_N$ between 10 and 76
   Hf concentration between 5,000 and 14,000 ppmw
   Th/U ratio between 0.2 and 4
   Eu/Eu* between 0.1 and 0.6
   Ti concentration between 2 and 24 ppmw

These criteria may be translated into a numeric scheme by employing a binary scoring system. A zircon will score 1 for each criterion it satisfies in categories (2) and (3). However, because inclusion phases have extraordinary controls on both Ce/Ce* and Ti-in-zircon temperatures, the criteria outlined in category (1) are given a 2x weight factor; that is to say, a zircon will receive a score of 2 for each criterion it satisfies in category (1). Conversely, if the zircon falls outside the predefined range, it receives a score of 0 for that proxy. For example, a zircon entry that satisfies all criteria except that its U/Nb > 20, La concentration > 0.1 ppmw, and $(Lu/Gd)_N$ < 10 ppmw will have a total score of 11 (Figure 8).

Because the filter scheme relies on multiple trace element measurements, analytical uncertainties at the boundary conditions of each criterion could lead to false negatives. For example, a zircon with an Hf concentration of 14,100 ppmw might be rejected by the filter criterion 5,000 < Hf < 14,000 ppmw, but the analytical uncertainty on the measured Hf abundance (e.g., 5% sd) may in fact overlap with the accepted range. Therefore, we recommend that uncertainties should be considered when applying the pass/fail chemical criteria described above. This study assumed and applied a 5% analytical uncertainty at the boundary conditions of each criterion.

The total score estimates the similarity of a given zircon entry to a mantle-equilibrated zircon. Zircon with high scores are more likely to represent mantle-equilibrated zircon, whereas zircon with low scores have a reduced probability of recording or preserving mantle signatures. Samples with the highest confidence of reflecting mantle-equilibrated zircon will have a maximum score of 15 (i.e., satisfying all criteria).

5. Establishment, Validation, and Application of Filter Scheme to Zircon Samples

The scores for all 2,173 zircon entries compiled here cover the entire scoring range from 1 to 15 (Figure 9). Application of Hoskin's differentiation diagrams suggests that the low score zircon are derived from hydrothermal sources, whereas high score zircon cluster within the magmatic domain (Figure 10). In general, the zircon population with the highest scores converges at melt redox states near the FMQ region.

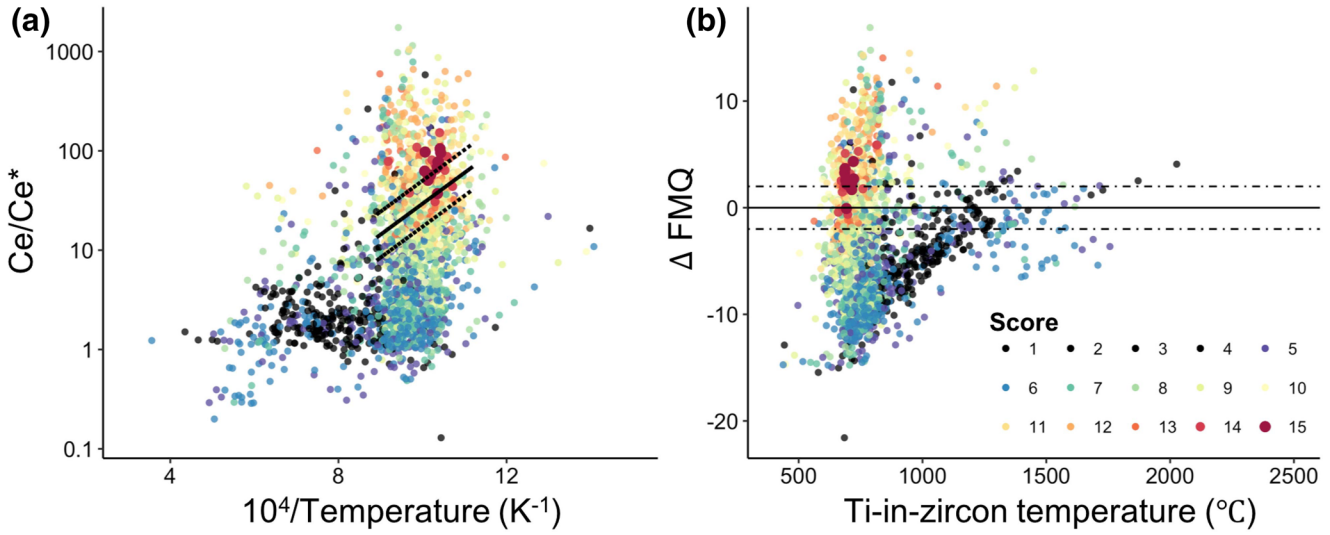

Figure 9. Application of the proposed filter scheme and scoring system to the zircon dataset compiled here (n = 2,173). In general, the large spread in observed Ce/Ce* may be attributed to distinct sources of source melts, magmatic differentiation prior to zircon saturation, and/or mineral inclusions in trace element measurements. The black dotted and solid lines represent ΔFMQ ± 2.

Based on the distributions of scores, the zircon may be divided into three groups, as described further below (Figure 11a).

5.1. Establishment of Multidimensional Filter Scheme

Group III zircon have scores ≤ 7 with a median oxygen fugacity ΔFMQ −5.7 ± 5.0 (± median absolute deviation; Figure 11a). Consequently, these samples are interpreted to represent nonmagmatic zircon. The median absolute deviation is calculated as the median of the absolute distances of each data value to the median of the whole sample set; compared to sd, this value is less affected by outliers and better represents statistical dispersion within dataset. Group III zircon generally yield Ce/Ce* approaching unity but

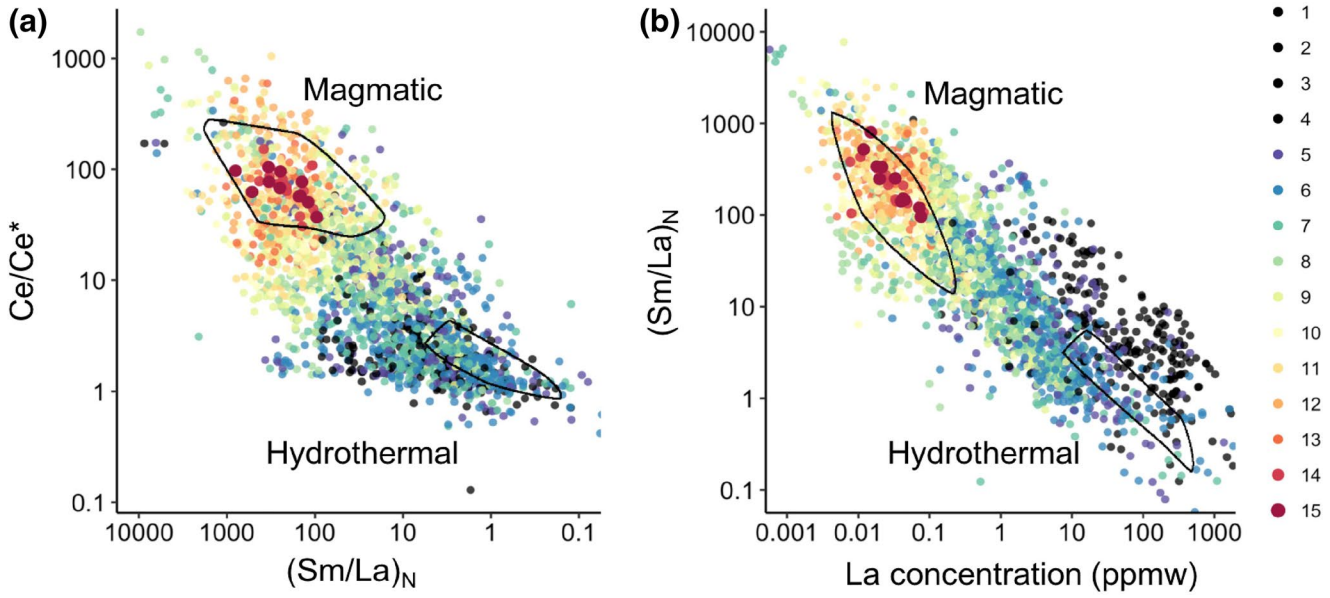

Figure 10. Distribution of the compiled zircon dataset within the preestablished magmatic and hydrothermal fields proposed by Hoskin (2005).

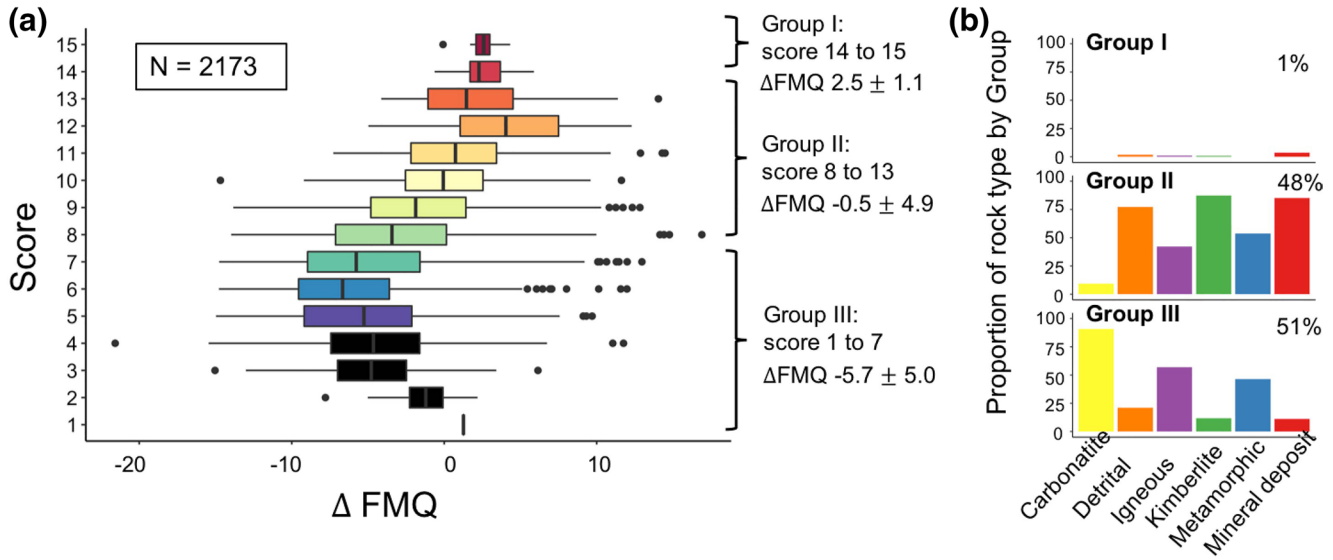

Figure 11. (a) Boxplots of zircon populations for each score. Based on the median and variance of inferred melt redox states, these populations may be divided into three groups: Group I (score 14–15), Group II (score 8–13), and Group III (score 1–7). (b) Selectivity and distribution of different rock types within each group. The percentage represents the proportion of all zircon that fall within each group.

surprisingly high Ti-in-zircon temperatures (> 1,000°C), highlighting unusual trace element characteristics (Figure 9). Group III zircon represent > 40% of zircon from metamorphic rocks and nearly all zircon from carbonatites (Figure 11b). According to the textures and morphologies of these samples provided in their source references, zircon with unity Ce/Ce* and high Ti-in-zircon temperatures are often associated with metamict, hydrothermal, and metamorphic zircon, which validate that Group III zircon represent nonmagmatic origins (Figure 12).

Group II zircon have scores from 8 to 13 with a median oxygen fugacity ΔFMQ −0.5 ± 4.9. They mostly represent zircon with mineral inclusions and zircon that crystallized from parental magma that interacted with hydrous fluids and/or surface materials. Group II zircon have Ti-in-zircon temperatures between 600°C and 850°C, in agreement with experiments and simulations of magmatic zircon crystallization temperature.

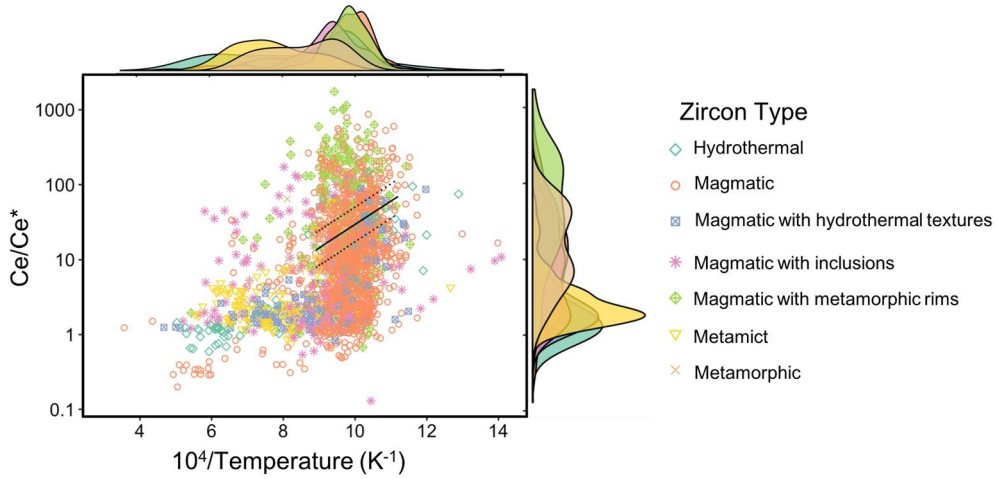

Figure 12. Plot of Ce/Ce* and temperature in zircon as a function of morphology and texture. The texture of each individual zircon was deduced from BSE and CL imaging from source references (see Supporting Information I for more details). The black dotted and solid lines represent FMQ 2. The density plots on the x- and y-axis use a kernel density estimation. BSE, back-scattered electron; CL, cathodoluminescence.

However, their Ce/Ce* ranges over three orders of magnitudes (Figure 9). Hoskin discriminant diagrams suggest the majority of Group II zircon extend from the magmatic zone toward hydrothermal signatures (Figure 10). Such a trend implies that Group II zircon may have had magmatic origins but fluid alteration and/or metamorphism conditions induced post-magmatic trace element diffusion, mineral exsolution, or inclusions that attenuated Ce/Ce* and diminished the original magmatic fingerprint.

Group II includes nearly all zircon derived from kimberlites, detrital zircon in sedimentary rocks (i.e., siltstone), mineral deposits, and ~40% zircon from igneous rocks (Figure 11b). According to the specific examples in this study, zircon in kimberlite are identified as xenocrysts with source melts of mafic composition (Kostrovitsky et al., 2016), and detrital zircon in siltstone are crystallized from melts of A-type granitoids or a mixture of felsic and mafic melts (Paulsen et al., 2017). Therefore, despite the range of host rock compositions, most of Group II zircon have a magmatic origin. Petrographic examination via BSE and CL images suggest most Group II samples have magmatic textures but with inclusions or secondary recrystallization features, likely resulting from hydrothermal fluids or metamorphism (Figure 12).

Group I zircon have scores from 14 to 15, meaning they have the highest confidence level of representing mantle-equilibrated zircon. The most noticeable differences between Group I and II zircon are the reduced variations in temperature and Ce/Ce*, and by extension inferred melt redox states (Figure 11a).

The majority of Group I zircon are from the rhyolitic Mesa Falls Tuff (MFT) at Yellowstone volcanic field (Rivera et al., 2016). The physical conditions and mechanisms of generating silicic magma at Yellowstone are hotly debated topics because cyclic caldera collapse, magma mixing, and crustal assimilation often overprint and complicate the signatures of minerals and magma (Bindeman & Valley, 2001; Wotzlaw et al., 2015). As a result, Yellowstone zircon often inherit heterogeneous oxygen isotopic compositions and trace element concentrations across zones that reflect variations in melt conditions as a function of time. Based on detailed petrographic observation, trace element composition, and U–Pb dating, Rivera et al. (2016) identified four Chemical Domains in MFT zircon that represent distinctive magma conditions; in general, Domains 1 and 2 represent magma mixing from hydrothermally altered crust (characterized by statistically distinct $\delta^{18}O$ below the mantle field); Domain 3 represents the oldest pristine magma in the zircon core; and, Domain 4 represents magma with significant fractionation. Out of > 400 zircon analyses, this filter scheme successfully isolated all zircon from Domains 1, 2, and 4, and highlighted zircon from Domain 3, sourced from the most primitive melt. Similarly, other Group I zircon include magmatic cores from Cu-Zn deposits (Zhu et al., 2017), detrital zircon in siltstone (Paulsen, 2017), and magmatic zircon from Yellowstone rhyolite (Colón et al., 2015). Although there are no oxygen isotopes for selected zircon grains as corroborative validation for their mantle-equilibrated source melts, all of these references have: (1) observed multistage growth of zircon and preservation of magmatic textures for some zircon; and, (2) underscored the likelihood of maintaining mantle-equilibrated source melt based on Hf and oxygen isotopes on limited zircon grains and whole rock.

Accordingly, this filter scheme has demonstrated the capacity to isolate nonmagmatic zircon (Group III zircon), magmatic zircon with inclusions or enriched source melt sources (Group II zircon), and mantle-equilibrated zircon (Group I). Based on the Group I zircon population from the compiled zircon dataset interrogated here, we infer a median mantle redox state of ΔFMQ 2.5 ± 1.1 (n = 23). This result overlaps with upper mantle redox values ΔFMQ ± 2 via $Fe^{3+}/\sum Fe$ on spinel peridotites (Frost & McCammon, 2008).

5.2. Validation of Filter Scheme With Jack Hills Zircon

We evaluate the performance of the proposed filter scheme using a suite of Jack Hills zircon (n = 53; data from Cavosie et al., 2006 and Fu et al., 2008). Because this dataset lacks Nb measurements, U/Yb and Th/Yb are used as alternative proxies to U/Nb and Th/Nb, respectively (see Section 3.2.2 for justification).

From this dataset, seven prospective mantle-equilibrated zircon emerged with the highest filter scores (Figure 13), six of which are also characterized by mantle-like oxygen isotopic signatures, oscillatory magmatic zoning, and typical magmatic trace element patterns (commonly referred as type 1 zircon), and sourced from a granitoid melt with > 70% SiO_2 according to classification and regression trees analysis (see Supporting Information I for detailed information). Five unselected zircon (score < 14) have mantle-like oxygen isotope signatures but exhibit patchy zoning and/or are estimated to have a source melt composition

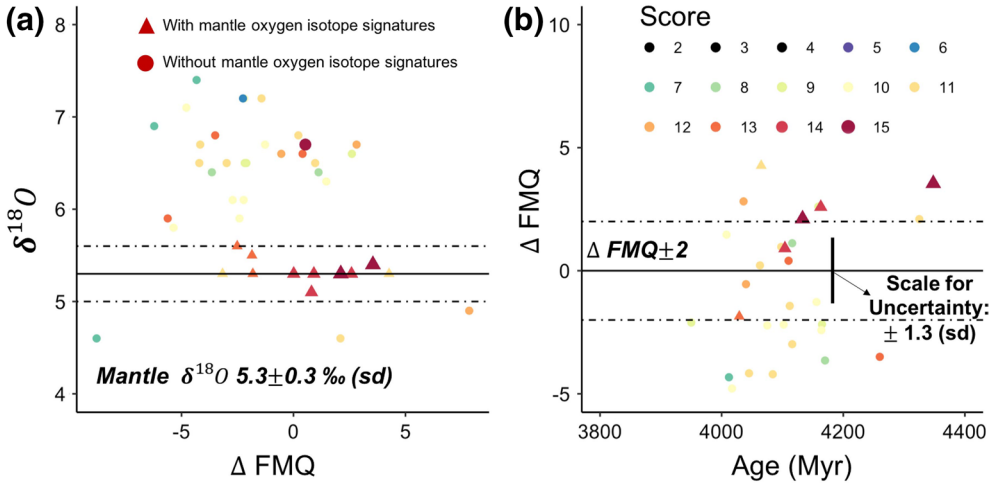

Figure 13. Application of the proposed filter scheme to a set of Jack Hills zircons (n = 53). (a) The black dotted and solid lines represent the mantle equilibrium state as $\delta^{18}O$ 5.3 ± 0.3 ‰ (sd; Valley et al., 1998). This filter scheme identified seven mantle-equilibrated zircons, six with mantle-like oxygen isotopes. The average Hadean magma oxygen fugacity is determined to be ΔFMQ1.5 ± 1.3 (sd) from these samples. (b) The black dotted and solid lines represent ΔFMQ ± 2.

with < 65% SiO_2. This contextual information implies they have experienced potential postmagmatic replacement and early zircon saturation in a less felsic source melt due to Zr enrichment from an open system behavior. The remaining 41 unselected zircon have oxygen isotope outside of mantle-equilibrium values and have score < 14.

In sum, this validation study highlights the sensitivity of proposed filter scheme at selecting mantle-equilibrated zircon. The average inferred melt redox state of the seven selected mantle-equilibrated zircon is ΔFMQ 1.5 ± 1.3 (sd), overlapping with the average oxygen fugacity ΔFMQ1.4 ± 2.3 (sd; $n = 5$) determined from the same dataset previously (Trail et al., 2011). We, therefore, consider this sd, 1.3 log units, as the external reproducibility of determining mantle redox states via the method provided in this study. Although the statistics are limited, these data suggest that the upper mantle may have been oxidized to FMQ region since 4,400 Ma.

5.3. Case Study: Application of Filter Scheme to Zircon From Greenland Rock Samples

As a final demonstration, this filter scheme is applied to zircon (n = 76) from three metasedimentary rocks (524906, 524907, and 524994) that sampled at Kangerdluarssuk Fjord, southern West Greenland (see Supporting Information II or refer to Dyck et al. (2015) for more details). Without further contextual information, this filter scheme is capable of providing valuable insights about the saturation history of zircon.

Based on distributions of the scores, all three classes of zircon (Groups I, II, and III) are recognized, implying multiple zircon populations in the host rocks. However, most zircon in these three samples are characterized as Group III, suggesting that the majority of samples has experienced significant degrees of hydrothermal alteration and/or metamorphism that led to recrystallization as nonmagmatic zircon (Figure 14). Sample 524994 has the lowest proportion of Group III zircon, indicating that this rock sample has experienced the least amount of modification. By using the trace element composition of the highest score zircon grain (the most likely mantle-equilibrated candidate), we infer a local mantle redox state of ΔFMQ −0.5 ± 1.3 circa 2,950 Ma (the age of the sample). The uncertainty of the melt redox state determination is adopted from Section 5.2. This result overlaps with the inferred Hadean upper mantle redox values from Section 5.2, suggesting that the upper mantle has oxidized to and maintained its redox states around FMQ region in the early Earth history.

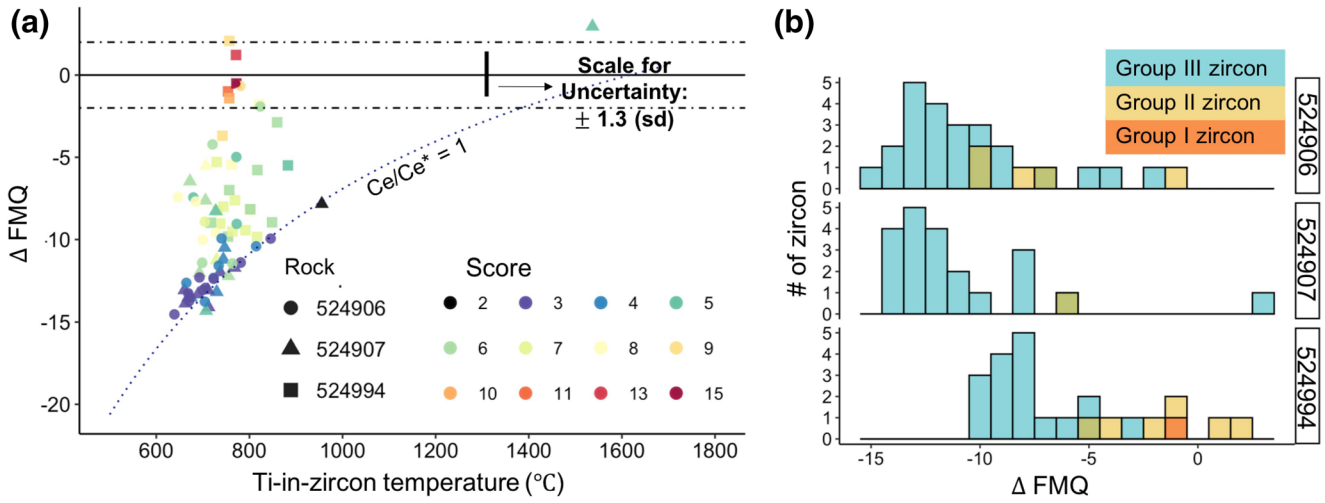

Figure 14. Application of the filter scheme proposed here to a case study of zircon from three metasedimentary rocks 524906, 524907, and 524994 (see Supporting Information I and II). (a) Inferred melt redox states as a function of temperature. (b) Distribution of zircon by groups.

6. Conclusions

We have established a simple filter scheme for selecting mantle-equilibrated zircon using only trace element systematics (P, Ti, Y, Nb, REE, Hf, Th, and U). This filter scheme has demonstrated the capacity to isolate nonmagmatic zircon (Group III scores ≤ 7), magmatic zircon with inclusions or derived from enriched source melt (Group II scores between 8 and 13), and mantle-equilibrated zircon (Group I scores ≥ 14). This filter scheme is validated by identifying mantle-equilibrated zircon from a well-characterized Jack Hills zircon dataset without requiring traditional protocols (i.e., petrographic studies, whole rocks analysis, and oxygen isotopes), and reproducing the mantle oxygen fugacity derived from previous studies, with an uncertainty of 1.3 log unit (sd). Further, the application of proposed filter scheme to zircon from three metasedimentary rocks implicates a mantle source ΔFMQ −0.5 ± 1.3 circa 2,950 Ma. Altogether, this study has established, validated, and demonstrated a filter scheme that can facilitate studies of out-of-context and in-context zircon in the future.

Data Availability Statement

The compiled 2,173 zircon dataset and the Hadean zircon dataset are acquired from previously published works, which are listed in the Supporting Information I. The Greenland zircon dataset was submitted to Earthchem (http://doi.org/10.26022/IEDA/111674) and also accessible in Supporting Information I.

Acknowledgments
This study was supported by the NASA grant (80NSSC18K1612) and the Carlsbergfondet grant that awarded to Adam Garde at the Geological Survey of Denmark and Greenland. My sincere gratitude goes to my coauthors and friends, Rick, Phil, and Barry for encouraging me taking over this project, helping me overcome obstacles, and maturing as a proto-scientist. I am looking forward to having more joyful conversations and many free coffees from them in the future. Thank you, Dr. Dustin Trail, Dr. Elizabeth Bell, and one anonymous reviewer for their constructive suggestions. We thank Tonny Thomsen, Bo Møller Stensgaard, and Brendan Dyck for analytical assistance.

References

Anderson, A., Wirth, R., & Thomas, R. (2008). The alteration of metamict zircon and its role in the remobilization of high-field-strength elements in the Georgeville granite, Nova Scotia. *Canadian Mineralogist*, *46*(1), 1–18. https://doi.org/10.3749/canmin.46.1.1

Arevalo, R., & McDonough, W. F. (2010). Chemical variations and regional diversity observed in MORB. *Chemical Geology*, *271*(1–2), 70–85. https://doi.org/10.1016/j.chemgeo.2009.12.013

Bea, F. (1996). Residence of REE, Y, Th and U in granites and crustal protoliths; implications for the chemistry of crustal melts. *Journal of Petrology*, *37*(3), 521–552. https://doi.org/10.1093/petrology/37.3.521

Bell, E. A., Boehnke, P., Barboni, M., & Harrison, T. M. (2019). Tracking chemical alteration in magmatic zircon using rare earth element abundances. *Chemical Geology*, *510*, 56–71. https://doi.org/10.1016/j.chemgeo.2019.02.027

Bell, E. A., Boehnke, P., Hopkins-Wielicki, M. D., & Harrison, T. M. (2015). Distinguishing primary and secondary inclusion assemblages in Jack Hills zircons. *Lithos*, *234–235*, 15–26. https://doi.org/10.1016/j.lithos.2015.07.014

Belousova, E. A., Griffin, W. L., O'Reilly, S. Y., & Fisher, N. I. (2002). Igneous zircon: Trace element composition as an indicator of source rock type. *Contributions to Mineralogy and Petrology*, *143*(5), 602–622. https://doi.org/10.1007/s00410-002-0364-7

Bindeman, I. N., & Valley, J. W. (2001). Low-δ18O Rhyolites from Yellowstone: Magmatic evolution based on analyses of zircons and individual phenocrysts. *Journal of Petrology*, *42*(8), 1491–1517. https://doi.org/10.1093/petrology/42.8.1491

Boehnke, P., Watson, E. B., Trail, D., Harrison, T. M., & Schmitt, A. K. (2013). Zircon saturation re-revisited. *Chemical Geology*, *351*, 324–334. https://doi.org/10.1016/J.CHEMGEO.2013.05.028

Borisov, A., & Aranovich, L. (2019). Zircon solubility in silicate melts: New experiments and probability of zircon crystallization in deeply evolved basic melts. *Chemical Geology*, *510*, 103–112. https://doi.org/10.1016/j.chemgeo.2019.02.019

Burnham, A. D., & Berry, A. J. (2012). An experimental study of trace element partitioning between zircon and melt as a function of oxygen fugacity. *Geochimica et Cosmochimica Acta*, *95*, 196–212. https://doi.org/10.1016/j.gca.2012.07.034

Burnham, A. D., & Berry, A. J. (2017). Formation of Hadean granites by melting of igneous crust. *Nature Geoscience*, *10*(6), 457–461. https://doi.org/10.1038/ngeo2942

Carley, T. L., Miller, C. F., Wooden, J. L., Padilla, A. J., Schmitt, A. K., Economos, R. C., et al. (2014). Iceland is not a magmatic analog for the Hadean: Evidence from the zircon record. *Earth and Planetary Science Letters*, *405*, 85–97. https://doi.org/10.1016/j.epsl.2014.08.015

Cavosie, A. J., Valley, J. W., & Wilde, S. A. (2006). Correlated microanalysis of zircon: Trace element, δ18O, and U–Th–Pb isotopic constraints on the igneous origin of complex> 3900 Ma detrital grains. *Geochimica et Cosmochimica Acta*, *70*(22), 5601–5616. https://doi.org/10.1016/j.gca.2006.08.011

Chapman, J. B., Gehrels, G. E., Ducea, M. N., Giesler, N., & Pullen, A. (2016). A new method for estimating parent rock trace element concentrations from zircon. *Chemical Geology*, *439*, 59–70. https://doi.org/10.1016/j.chemgeo.2016.06.014

Chou, M. (1978). Calibration of oxygen buffers at elevated P and T using the hydration fugacity sensor. *American Mineralogist*, *63*, 690–703.

Claiborne, L. L., Miller, C. F., Flanagan, D. M., Clynne, M. A., & Wooden, J. L. (2010). Zircon reveals protracted magma storage and recycling beneath Mount St. Helens. *Geology*, *38*(11), 1011–1014. https://doi.org/10.1130/G31285.1

Claiborne, L. L., Miller, C. F., Walker, B. A., Wooden, J. L., Mazdab, F. K., & Bea, F. (2006). Tracking magmatic processes through Zr/Hf ratios in rocks and Hf and Ti zoning in zircons: An example from the Spirit mountain batholith, Nevada. *Mineralogical Magazine*, *70*(5), 517–543. https://doi.org/10.1180/0026461067050348

Colón, D. P., Bindeman, I. N., Ellis, B. S., Schmitt, A. K., & Fisher, C. M. (2015). Hydrothermal alteration and melting of the crust during the Columbia River Basalt-Snake River Plain transition and the origin of low-δ18O rhyolites of the central Snake River Plain. *Lithos*, *224–225*, 310–323. https://doi.org/10.1016/j.lithos.2015.02.022

Corfu, F., Hanchar, J. M., Hoskin, P. W. O., & Kinny, P. (2003). Atlas of zircon textures. *Reviews in Mineralogy and Geochemistry*, *53*(1), 469–500. https://doi.org/10.2113/0530469

Dyck, B., Reno, B. L., & Kokfelt, T. F. (2015). The Majorqaq Belt: A record of Neoarchaean orogenesis during final assembly of the North Atlantic craton, southern West Greenland. *Lithos*, *220–223*, 253–271. https://doi.org/10.1016/j.lithos.2015.01.024

Ferry, J. M., & Watson, E. B. (2007). New thermodynamic models and revised calibrations for the Ti-in-zircon and Zr-in-rutile thermometers. *Contributions to Mineralogy and Petrology*, *154*(4), 429–437. https://doi.org/10.1007/s00410-007-0201-0

Frost, D. J., & McCammon, C. A. (2008). The Redox state of Earth's mantle. *Annual Review of Earth and Planetary Sciences*, *36*(1), 389–420. https://doi.org/10.1146/annurev.earth.36.031207.124322

Frost, D. J., Mann, U., Asahara, Y., & Rubie, D. C. (2008). The redox state of the mantle during and just after core formation. *Philosophical Transactions of the Royal Society A: Mathematical, Physical and Engineering Sciences*, *366*(1883), 4315–4337. https://doi.org/10.1098/rsta.2008.0147

Fu, B., Page, F. Z., Cavosie, A. J., Fournelle, J., Kita, N. T., Lackey, J. S., et al. (2008). Ti-in-zircon thermometry: Applications and limitations. *Contributions to Mineralogy and Petrology*, *156*(2), 197–215. https://doi.org/10.1007/s00410-008-0281-5

Grimes, C. B., John, B. E., Kelemen, P. B., Mazdab, F. K., Wooden, J. L., Cheadle, M. J., et al. (2007). Trace element chemistry of zircons from oceanic crust: A method for distinguishing detrital zircon provenance. *Geology*, *35*(7), 643. https://doi.org/10.1130/G23603A.1

Grimes, C. B., Wooden, J. L., Cheadle, M. J., & John, B. E. (2015). "Fingerprinting" tectono-magmatic provenance using trace elements in igneous zircon. *Contributions to Mineralogy and Petrology*, *170*(5–6), 46. https://doi.org/10.1007/s00410-015-1199-3

Hanchar, J. M., & Watson, E. B. (2003). Zircon saturation thermometry. *Reviews in Mineralogy and Geochemistry*, *53*(1), 89–112. https://doi.org/10.2113/0530089

Harrison, T. M., Watson, E. B., & Aikman, A. B. (2007). Temperature spectra of zircon crystallization in plutonic rocks. *Geology*, *35*(7), 635–638. https://doi.org/10.1130/G23505A.1

Hawkesworth, C. J., & Kemp, A. I. S. (2006). Using hafnium and oxygen isotopes in zircons to unravel the record of crustal evolution. *Chemical Geology*, *226*(3–4), 144–162. https://doi.org/10.1016/j.chemgeo.2005.09.018

Hofmann, A. E., Baker, M. B., & Eiler, J. M. (2014). Sub-micron-scale trace-element distributions in natural zircons of known provenance: Implications for Ti-in-zircon thermometry. *Contributions to Mineralogy and Petrology*, *168*, 1057. https://doi.org/10.1007/s00410-014-1057-8

Hoskin, P. W. O., & Black, L. P. (2002). Metamorphic zircon formation by solid-state recrystallization of protolith igneous zircon. *Journal of Metamorphic Geology*, *18*(4), 423–439. https://doi.org/10.1046/j.1525-1314.2000.00266.x

Hoskin, P. W. O., & Ireland, T. R. (2000). Rare earth element chemistry of zircon and its use as a provenance indicator. *Geology*, *28*(7), 627–630. https://doi.org/10.1130/0091-7613(2000)028<0627:REECOZ>2.3.CO;2

Hoskin, P. W. O., & Schaltegger, U. (2003). The composition of zircon and igneous and metamorphic petrogenesis. *Reviews in Mineralogy and Geochemistry*, *53*(1), 27–62. https://doi.org/10.1046/j.1525-1314.2000.00266.x

Hoskin, P. W. O. (2005). Trace-element composition of hydrothermal zircon and the alteration of Hadean zircon from the Jack Hills, Australia. *Geochimica et Cosmochimica Acta*, *69*(3), 637–648. https://doi.org/10.1016/j.gca.2004.07.006

Janoušek, V., Holub, F. V., Verner, K., Čopjaková, R., Gerdes, A., Hora, J. M., et al. (2019). Two-pyroxene syenitoids from the Moldanubian Zone of the Bohemian Massif: Peculiar magmas derived from a strongly enriched lithospheric mantle source. *Lithos*, *342–343*, 239–262. https://doi.org/10.1016/j.lithos.2019.05.028

Kelly, N. M., & Harley, S. L. (2005). An integrated microtextural and chemical approach to zircon geochronology: Refining the Archaean history of the Napier complex, east Antarctica. *Contributions to Mineralogy and Petrology*, *149*(1), 57–84. https://doi.org/10.1007/s00410-004-0635-6

Kirkland, C. L., Smithies, R. H., Taylor, R. J. M., Evans, N., & McDonald, B. (2015). Zircon Th/U ratios in magmatic environs. *Lithos*, *212–215*, 397–414. https://doi.org/10.1016/j.lithos.2014.11.021

Kostrovitsky, S. I., Skuzovatov, S. Y., Yakovlev, D. A., Sun, J., Nasdala, L., & Wu, F. Y. (2016). Age of the Siberian craton crust beneath the northern kimberlite fields: Insights to the craton evolution. *Gondwana Research*, *39*, 365–385. https://doi.org/10.1016/j.gr.2016.01.008

Kump, L. R., Kasting, J. F., & Barley, M. E. (2001). Rise of atmospheric oxygen and the "upside-down" Archean mantle. *Geochemistry, Geophysics, Geosystems*, *2*(1), 1525–2027. https://doi.org/10.1029/2000gc000114

Lee, C. T. A., & Bachmann, O. (2014). How important is the role of crystal fractionation in making intermediate magmas? Insights from Zr and P systematics. *Earth and Planetary Science Letters*, *393*, 266–274. https://doi.org/10.1016/j.epsl.2014.02.044

Linnen, R. L., & Keppler, H. (2002). Melt composition control of Zr/Hf fractionation in magmatic processes. *Geochimica et Cosmochimica Acta*, *66*(18), 3293–3301. https://doi.org/10.1016/S0016-7037(02)00924-9

Loucks, R. R., Fiorentini, M. L., & Henríquez, G. J. (2020). New magmatic oxybarometer using trace elements in zircon. *Journal of Petrology*, *61*(3), egaa034. https://doi.org/10.1093/petrology/egaa034
McCammon, C. (2005). Geochemistry: The Paradox of mantle Redox. *Science*, *308*(5723), 807–808. https://doi.org/10.1126/science.1110532
McDonough, W. F., & Sun, S. S. (1995). The composition of the Earth. *Chemical Geology*, *120*(3–4), 223–253. https://doi.org/10.1016/0009-2541(94)00140-4
Mysen, B. O., Holtz, F., Pichavant, M., Beny, J. M., & Montel, J. M. (1997). Solution mechanisms of phosphorus in quenched hydrous and anhydrous granitic glass as a function of peraluminosity. *Geochimica et Cosmochimica Acta*, *61*(18), 3913–3926. https://doi.org/10.1016/S0016
Nandedkar, R. H., Ulmer, P., & Müntener, O. (2014). Fractional crystallization of primitive, hydrous arc magmas: An experimental study at 0.7 GPa. *Contributions to Mineralogy and Petrology*, *167*(6), 1–27. https://doi.org/10.1007/s00410-014-1015-5
Page, F. Z., Fu, B., Kita, N. T., Fournelle, J., Spicuzza, M. J., Schulze, D. J., et al. (2007). Zircons from kimberlite: New insights from oxygen isotopes, trace elements, and Ti in zircon thermometry. *Geochimica et Cosmochimica Acta*, *71*(15), 3887–3903. https://doi.org/10.1016/j.gca.2007.04.031
Paulsen, T., Deering, C., Sliwinski, J., Bachmann, O., & Guillong, M. (2017). New detrital zircon age and trace element evidence for 1450 Ma igneous zircon sources in East Antarctica. *Precambrian Research*, *300*, 53–58. https://doi.org/10.1016/j.precamres.2017.07.011
Pupin, J.-P. (2000). Granite genesis related to geodynamics from Hf-Y in zircon. *Earth and Environmental Science Transactions of the Royal Society of Edinburgh*, *91*(1–2), 245–256. https://doi.org/10.1017/S0263593300007410
Rivera, T. A., Schmitz, M. D., Jicha, B. R., & Crowley, J. L. (2016). Zircon petrochronology and 40Ar/39Ar sanidine dates for the mesa falls tuff: Crystal-scale records of magmatic evolution and the short lifespan of a large yellowstone magma chamber. *Journal of Petrology*, *57*(9), 1677–1704. https://doi.org/10.1093/petrology/egw053
Robinson, F. A., Foden, J. D., & Collins, A. S. (2015). Zircon geochemical and geochronological constraints on contaminated and enriched mantle sources beneath the Arabian shield, Saudi Arabia. *Journal of Geology*, *123*(5), 463–489. https://doi.org/10.1086/683192
Rubatto, D., & Hermann, J. (2007). Experimental zircon/melt and zircon/garnet trace element partitioning and implications for the geochronology of crustal rocks. *Chemical Geology*, *241*(1–2), 38–61. https://doi.org/10.1016/j.chemgeo.2007.01.027
Rubatto, D. (2017). Zircon: The metamorphic mineral. *Reviews in Mineralogy and Geochemistry*, *83*(1), 261–295. https://doi.org/10.2138/rmg.2017.83.9
Rudnick, R. L. (1995). Making continental crust. *Nature*, *378*(6557), 571–578. https://doi.org/10.1038/378571a0
Samperton, K. M., Bell, E. A., Barboni, M., Brenhin Keller, C., & Schoene, B. (2017). Zircon age-temperature-compositional spectra in plutonic rocks. *Geology*, *45*(11), 983–986. https://doi.org/10.1130/G38645.1
Sawaki, Y., Suzuki, K., Asanuma, H., Okabayashi, S., Hattori, K., Saito, T., & Hirata, T. (2017). Geochemical characteristics of zircons in the Ashizuri A-type granitoids: An additional granite topology tool for detrital zircon studies. *Island Arc*, *26*(6), e12216. https://doi.org/10.1111/iar.12216
Shao, T., Xia, Y., Ding, X., Cai, Y., & Song, M. (2019). Zircon saturation in terrestrial basaltic melts and its geological implications. *Solid Earth Sciences*, *4*(1), 27–42. https://doi.org/10.1016/j.sesci.2018.08.001
Siégel, C., Bryan, S. E., Allen, C. M., & Gust, D. A. (2018). Use and abuse of zircon-based thermometers: A critical review and a recommended approach to identify antecrystic zircons. *Earth-Science Reviews*, *176*, 87–116. https://doi.org/10.1016/J.EARSCIREV.2017.08.011
Smythe, D. J., & Brenan, J. M. (2015). Cerium oxidation state in silicate melts: Combined fO2, temperature and compositional effects. *Geochimica et Cosmochimica Acta*, *170*, 173–187. https://doi.org/10.1016/j.gca.2015.07.016
Smythe, D. J., & Brenan, J. M. (2016). Magmatic oxygen fugacity estimated using zircon-melt partitioning of cerium. *Earth and Planetary Science Letters*, *453*, 260–266. https://doi.org/10.1016/j.epsl.2016.08.013
Spandler, C., Hermann, J., & Rubatto, D. (2004). Exsolution of thortveitite, yttrialite and xenotime during low temperature recrystallization of zircon from New Caledonia, and their significance for trace element incorporation in Nanogranitoids and crustal melting View project Magma fertility for Au-Cu, petrogenesis and geodynamic setting of Carboniferous and Permian magmatic complexes (Queensland, Australia) View project. *American Mineralogist*, *89*, 1795–1806. https://doi.org/10.2138/am-2004-11-1226
Spencer, C. J., Cavosie, A. J., Raub, T. D., Rollinson, H., Jeon, H., Searle, M. P., et al. (2017). Evidence for melting mud in Earth's mantle from extreme oxygen isotope signatures in zircon. *Geology*, *45*(11), 975–978. https://doi.org/10.1130/G39402.1
Sun, J., Tappe, S., Kostrovitsky, S. I., Liu, C. Z., Skuzovatov, S. Y., & Wu, F. Y. (2018). Mantle sources of kimberlites through time: A U-Pb and Lu-Hf isotope study of zircon megacrysts from the Siberian diamond fields. *Chemical Geology*, *479*, 228–240. https://doi.org/10.1016/j.chemgeo.2018.01.013
Tang, M., Erdman, M., Eldridge, G., & Lee, C. T. A. (2018). The redox "filter" beneath magmatic orogens and the formation of continental crust. *Science Advances*, *4*(5). https://doi.org/10.1126/sciadv.aar4444
Taylor, R. J. M., Harley, S. L., Hinton, R. W., Elphick, S., Clark, C., & Kelly, N. M. (2015). Experimental determination of REE partition coefficients between zircon, garnet and melt: A key to understanding high-T crustal processes. *Journal of Metamorphic Geology*, *33*(3), 231–248. https://doi.org/10.1111/jmg.12118
Tichomirowa, M., Whitehouse, M. J., Gerdes, A., Götze, J., Schulz, B., & Belyatsky, B. V. (2013). Different zircon recrystallization types in carbonatites caused by magma mixing: Evidence from U-Pb dating, trace element and isotope composition (Hf and O) of zircons from two Precambrian carbonatites from Fennoscandia. *Chemical Geology*, *353*, 173–198. https://doi.org/10.1016/j.chemgeo.2012.11.004
Trail, D., Bruce Watson, E., & Tailby, N. D. (2012). Ce and Eu anomalies in zircon as proxies for the oxidation state of magmas. *Geochimica et Cosmochimica Acta*, *97*, 70–87. https://doi.org/10.1016/J.GCA.2012.08.032
Trail, D., Mojzsis, S. J., Harrison, T. M., Schmitt, A. K., Watson, E. B., & Young, E. D. (2007). Constraints on Hadean zircon protoliths from oxygen isotopes, Ti-thermometry, and rare earth elements. *Geochemistry, Geophysics, Geosystems*, *8*(6). https://doi.org/10.1029/2006GC001449
Trail, D., Tailby, N., Wang, Y., Mark Harrison, T., & Boehnke, P. (2017). Aluminum in zircon as evidence for peraluminous and metaluminous melts from the Hadean to present. *Geochemistry, Geophysics, Geosystems*, *18*(4), 1580–1593. https://doi.org/10.1002/2016GC006794
Trail, D., Watson, E. B., & Tailby, N. D. (2011). The oxidation state of Hadean magmas and implications for early Earth's atmosphere. *Nature*, *480*(7375), 79–82. https://doi.org/10.1038/nature10655
Valley, J. W., Kinny, P. D., Schulze, D. J., & Spicuzza, M. J. (1998). Zircon megacrysts from kimberlite: Oxygen isotope variability among mantle melts. *Contributions to Mineralogy and Petrology*, *133*(1–2), 1–11. https://doi.org/10.1007/s004100050432
Vilalva, F. C. J., Simonetti, A., & Vlach, S. R. F. (2019). Insights on the origin of the Graciosa A-type granites and syenites (Southern Brazil) from zircon U-Pb geochronology, chemistry, and Hf and O isotope compositions. *Lithos*, *340–341*, 20–33. https://doi.org/10.1016/j.lithos.2019.05.001
Wang, X., Griffin, W. L., & Chen, J. (2010). Hf contents and Zr/Hf ratios in granitic zircons. *Geochemical Journal*, *44*(1), 65–72. https://doi.org/10.2343/geochemj.1.0043

Wang, Q., Zhu, D. C., Zhao, Z. D., Guan, Q., Zhang, X. Q., Sui, Q. L., et al. (2012). Magmatic zircons from I-, S- and A-type granitoids in Tibet: Trace element characteristics and their application to detrital zircon provenance study. *Journal of Asian Earth Sciences*, *53*, 59–66. https://doi.org/10.1016/j.jseaes.2011.07.027

Watson, E. B., & Harrison, T. M. (2005). Zircon thermometer Reveals minimum melting conditions on Earliest earth. *Science*, *308*(5723), 841–844. https://doi.org/10.1126/science.1110265

Watson, E. B., Wark, D. A., & Thomas, J. B. (2006). Crystallization thermometers for zircon and rutile. *Contributions to Mineralogy and Petrology*, *151*(4), 413–433. https://doi.org/10.1007/s00410-006-0068-5

Watson, E. B. (1979). Zircon saturation in felsic liquids: Experimental results and applications to trace element geochemistry. *Contributions to Mineralogy and Petrology*, *70*(4), 407–419. https://doi.org/10.1007/BF00371047

Whitehouse, M. J., & Platt, J. P. (2003). Dating high-grade metamorphism - Constraints from rare-earth elements in zircon and garnet. *Contributions to Mineralogy and Petrology*, *145*(1), 61–74. https://doi.org/10.1007/s00410-002-0432-z

Wotzlaw, J. F., Bindeman, I. N., Stern, R. A., D'Abzac, F. X., & Schaltegger, U. (2015). Rapid heterogeneous assembly of multiple magma reservoirs prior to Yellowstone supereruptions. *Scientific Reports*, *5*, 14026. https://doi.org/10.1038/srep14026

Xiang, W., Griffin, W. L., Chen, J., Huang, P., & Li, X. (2011). U and Th contents and Th/U Ratios of zircon in felsic and mafic magmatic Rocks: Improved zircon-melt distribution coefficients. *Acta Geologica Sinica*, *85*(1), 164–174. https://doi.org/10.1111/j.1755-6724.2011.00387.x

Yakymchuk, C., Kirkland, C. L., & Clark, C. (2018). Th/U ratios in metamorphic zircon. *Journal of Metamorphic Geology*, *36*(6), 715–737. https://doi.org/10.1111/jmg.12307

Yang, X., Gaillard, F., & Scaillet, B. (2014). A relatively reduced Hadean continental crust and implications for the early atmosphere and crustal rheology. *Earth and Planetary Science Letters*, *393*, 210–219. https://doi.org/10.1016/J.EPSL.2014.02.056

Zheng, J., Griffin, L., O'Reilly, S. Y., Lu, F., Yu, C., Zhang, M., & Li, H. (2004). U-Pb and Hf-isotope analysis of zircons in mafic from Fuxian kimberlites: Evolution of the lower crust beneath the North China craton. *Contributions to Mineralogy and Petrology*, *148*(1), 79–103. https://doi.org/10.1007/s00410-004-0587-x

Zhong, S., Feng, C., Seltmann, R., Li, D., & Dai, Z. (2018a). Geochemical contrasts between late Triassic ore-bearing and barren intrusions in the Weibao Cu–Pb–Zn deposit, east Kunlun Mountains, NW China: Constraints from accessory minerals (zircon and apatite). *Mineralium Deposita*, *53*(6), 855–870. https://doi.org/10.1007/s00126-017-0787-8

Zhong, S., Feng, C., Seltmann, R., Li, D., & Qu, H. (2018b). Can magmatic zircon be distinguished from hydrothermal zircon by trace element composition? The effect of mineral inclusions on zircon trace element composition. *Lithos*, *314–315*, 646–657. https://doi.org/10.1016/j.lithos.2018.06.029

Zhu, M., Zhang, L., Dai, Y., Wang, C., & Peng, Z. (2017). Hydrothermal modification of zircon geochemistry and Lu–Hf isotopes from the Hongtoushan Cu–Zn deposit, China. *Ore Geology Reviews*, *86*, 707–718. https://doi.org/10.1016/j.oregeorev.2017.03.028

References from Supporting Information

Akinin, V. V., Andronikov, A. V., Mukasa, S. B., & Miller, E. L. (2013). Cretaceous lower crust of the continental margins of the Northern Pacific: Petrological and geochronological data on lower to middle crustal xenoliths. *Petrology*, *21*(1), 28–65. https://doi.org/10.1134/S0869591113010013

Cai, K., Sun, M., Xiao, W., Yuan, C., Zhao, G., Long, X., et al. (2014). Petrogenesis of late Paleozoic tholeiitic, Nb-enriched, calc-alkaline and adakitic rocks in southwestern Mongolia: Implications for intra-oceanic arc evolution. *Lithos*, *202–203*, 413–428. https://doi.org/10.1016/j.lithos.2014.06.004

Deer, W. A., Howie, R. A., & Zussman, J. (1992).An introduction to the rock-forming minerals, Vol. 2. Hong Kong: Longman Scientific & Technical. https://doi.org/10.1180/DHZ

Doroshkevich, A. G., Prokopyev, I. R., Izokh, A. E., Klemd, R., Ponomarchuk, A. V., Nikolaeva, I. V., & Vladykin, N. V. (2018). Isotopic and trace element geochemistry of the Seligdar magnesiocarbonatites (South Yakutia, Russia): Insights regarding the mantle evolution beneath the Aldan-Stanovoy shield. *Journal of Asian Earth Sciences*, *154*, 354–368. https://doi.org/10.1016/j.jseaes.2017.12.030

Dou, J., Siebel, W., He, J., & Chen, F. (2019). Different melting conditions and petrogenesis of peraluminous granites in western Qinling, China, and tectonic implications. *Lithos*, *336–337*, 97–111. https://doi.org/10.1016/j.lithos.2019.04.003

El-Bialy, M. Z., & Ali, K. A. (2013). Zircon trace element geochemical constraints on the evolution of the Ediacaran (600-614Ma) post-collisional Dokhan volcanics and Younger granites of SE Sinai, NE Arabian-Nubian shield. *Chemical Geology*, *360–361*, 54–73. https://doi.org/10.1016/j.chemgeo.2013.10.009

Frei, D., & Gerdes, A. (2009). Precise and accurate in situ U–Pb dating of zircon with high sample throughput by automated LA-SF-ICPMS. *Chemical Geology*, *261*, 261–270. https://doi.org/10.1016/j.chemgeo.2008.07.025

Frei, D., Hollis, J. A., Gerdes, A., Harlov, D., Karlsson, D., Vasques, P., et al. (2006). Advanced in situ trace element and geochronological microanalysis of geomaterials by laser ablation techniques. *Geological Survey of Denmark and Greenland Survey Bulletin*, *10*, 25–28. https://doi.org/10.34194/geusb.v10.4884

Kay, S. M., Jicha, B. R., Citron, G. L., Kay, R. W., Tibbetts, A. K., & Rivera, T. A. (2019). The Calc-alkaline Hidden Bay and Kagalaska Plutons and the construction of the central Aleutian oceanic arc crust. *Journal of Petrology*, *60*(2), 393–439. https://doi.org/10.1093/petrology/egy119

Li, H., Wu, J. H., Evans, N. J., Jiang, W. C., & Zhou, Z. K. (2018). Zircon geochronology and geochemistry of the Xianghualing A-type granitic rocks: Insights into multi-stage Sn-polymetallic mineralization in South China. *Lithos*, *312–313*, 1–20. https://doi.org/10.1016/j.lithos.2018.05.001

Liu, L., Hu, R. Z., Zhong, H., Tang, Y. W., Yang, J. H., Li, Z., et al. (2018). New constraints on the Cretaceous geodynamics of paleo-Pacific plate subduction: Insights from the Xiaojiang–Beizhang granitoids, Zhejiang Province, southeast China. *Lithos*, *314–315*, 382–399. https://doi.org/10.1016/j.lithos.2018.06.020

Lu, L., Qin, Y., Li, Z. F., Yan, L. L., Jin, X., & Zhang, K. J. (2019). Diachronous closure of the Shuanghu Paleo-Tethys ocean: Constraints from the late Triassic Tanggula arc-related volcanism in the east Qiangtang subterrane, central Tibet. *Lithos*, *328–329*, 182–199. https://doi.org/10.1016/j.lithos.2019.01.034

Lukács, R., Harangi, S., Bachmann, O., Guillong, M., Danišík, M., Buret, Y., et al. (2015). Zircon geochronology and geochemistry to constrain the youngest eruption events and magma evolution of the Mid-Miocene ignimbrite flare-up in the Pannonian Basin, eastern central Europe. *Contributions to Mineralogy and Petrology*, *170*(5–6), 1–26. https://doi.org/10.1007/s00410-015-1206-8

Pearce, N. J., Perkins, W. T., Westgate, J. A., Gorton, M. P., Jackson, S. E., Neal, C. R., & Chenery, S.P. (1997). A compilation of new and published major and trace element data for NIST SRM 610 and NIST SRM 612 glass reference materials. *Geostandards Newsletter*, *21*, 115–144. https://doi.org/10.1111/j.1751-908X.1997.tb00538.x

Poletti, J. E., Cottle, J. M., Hagen-Peter, G. A., & Lackey, J. S. (2016). Petrochronological constraints on the origin of the Mountain Pass ultrapotassic and carbonatite intrusive suite, California. *Journal of Petrology*, *57*(8), 1555–1598. https://doi.org/10.1093/petrology/egw050

Slezak, P., & Spandler, C. (2019). Carbonatites as recorders of mantle-derived magmatism and subsequent tectonic events: An example of the Gifford Creek Carbonatite Complex, Western Australia. *Lithos*, *328–329*, 212–227. https://doi.org/10.1016/j.lithos.2019.01.028

Verbaas, J., Thorkelson, D. J., Milidragovic, D., Crowley, J. L., Foster, D., Daniel Gibson, H., & Marshall, D. D. (2018). Rifting of western Laurentia at 1.38 Ga: The Hart River sills of Yukon, Canada. *Lithos*, *316–317*, 243–260. https://doi.org/10.1016/j.lithos.2018.06.018

Wang, Q., Chung, S. L., Li, X. H., Wyman, D., Li, Z. X., Sun, W. D., et al. (2012). Crustal melting and flow beneath northern Tibet: Evidence from mid-miocene to quaternary strongly peraluminous rhyolites in the Southern Kunlun Range. *Journal of Petrology*, *53*(12), 2523–2566. https://doi.org/10.1093/petrology/egs058

Yang, W. B., Niu, H. C., Shan, Q., Sun, W. D., Zhang, H., Li, N. B., et al. (2014). Geochemistry of magmatic and hydrothermal zircon from the highly evolved Baerzhe alkaline granite: Implications for Zr–REE–Nb mineralization. *Mineralium Deposita*, *49*(4), 451–470. https://doi.org/10.1007/s00126-013-0504-1

Zhang, S. H., Zhao, Y., Yang, Z. Y., He, Z. F., & Wu, H. (2009). The 1.35 Ga diabase sills from the northern North China Craton: Implications for breakup of the Columbia (Nuna) supercontinent. *Earth and Planetary Science Letters*, *288*(3–4), 588–600. https://doi.org/10.1016/j.epsl.2009.10.023

Zhao, L., Guo, F., Fan, W., Zhang, Q., Wu, Y., Li, J., & Yan, W. (2016). Early Cretaceous potassic volcanic rocks in the Jiangnan Orogenic Belt, East China: Crustal melting in response to subduction of the Pacific-Izanagi ridge? *Chemical Geology*, *437*, 30–43. https://doi.org/10.1016/j.chemgeo.2016.05.011